



Georg Rudelstorfer, BSc

**Construction and scale up of a Taylor-Couette Disc Contactor:
including installation, placing in operation, holdup measurements
and determination of drop size distribution**

MASTER'S THESIS

to achieve the university degree of

Diplom-Ingenieur

Master's degree programme: Chemical and Process Engineering

submitted to

Graz University of Technology

Supervisor

Univ. Prof. Dipl.-Ing Dr. techn. Matthäus Siebenhofer
Institute of Chemical Engineering and Environmental Technology

Co-Supervisor:

Dipl.-Ing. Annika Graftschaffer
Institute of Chemical Engineering and Environmental Technology

AFFIDAVIT

I declare that I have authored this thesis independently, that I have not used other than the declared sources/resources, and that I have explicitly indicated all material which has been quoted either literally or by content from the sources used. The text document uploaded to TUGRAZonline is identical to the present master's thesis.

Date

Signature

"It always seems impossible until its done."

(Nelson Mandela)

Acknowledgement

First of all i would like to thank Annika Graftschafter for great support over the whole time. She always had time for meetings and gave me motivation to finish writing of this thesis. A lot of projects followed after the construction of the TCDC 300. I always enjoyed working with Annika no matter if constructing a column that can handle three phase flow or spending one week on the Achema to represent the institute and show the world how the future of liquid-liquid extraction works. Thank you Annika for this great time.

Special thanks to Prof. Matthäus Siebenhofer for giving me the chance to be part of this great development. It is not self-evident to work in such a free and appreciatively atmosphere. Mr. Siebenhofer always lend an ear for questions and problems no matter about the topic. Thanks for understanding my situation and the responsibility I had as chair person of student's union at the TU Graz.

Thanks to the whole team of the Institute of Chemical Engineering and Eviromental Technology. I started working for the Institute in 2015 and never regret. The whole team and the atmosphere motivates to purse the goal.

Thanks to all my colleagues for the great time in my studies. Thanks to the whole team of student's union at the TU Graz. It was a instructive and sometimes exhausting time. But the things I learned in this time are amazing. I got the chance to be the chair person from 2017 to 2019. Thanks for this great time and big thanks to my team.

Thanks to my family for supporting me over the whole time. Thanks that i got the possibility to live out all my different interests in this time. I appreciate that very much.

Abstract

In this master thesis a stirred liquid-liquid extraction column called Taylor-Couette Disc Contactor in pilot scale was constructed and placed in operation. The geometric design of the column is based on the design rules according to Aksamija [1]. The column has a diameter of 300 mm and the active mixing zone has a height of 1 m. For hydrodynamic investigation, the drop size distribution was determined and the dispersed phase holdup was measured. The Taylor-Couette Disc Contactor (TCDC) is a very simple and promising design for agitated liquid-liquid extraction columns. The hydrodynamics in a TCDC have already been investigated in a 100 mm column. Examination of this by factor three scaled up column provides information on the scalability of the TCDC design. The test system used for all experiments is water and ShellSol-T (kerosene). Water is used for the continuous phase and ShellSol-T is used for the dispersed phase. The TCDC design is based on the design of the Rotating Disc Contactor (RDC), but without stator rings and with an increased shaft and disc diameter. The shaft diameter is increased to an optimal ratio of $D/d_{SH} = 0.5$ to prevent the formation of hydrodynamic dead zones around the shaft and in order to induce banded two-phase flow as formed in a Taylor-Couette reactor. TCDC columns are able to handle high hydraulic loads beyond $30 \text{ m}^3\text{m}^{-2}\text{h}^{-1}$. For the column design, certain knowledge of hydraulics is needed. For this, data of dispersed phase holdup (φ) and drop size distribution (DSD) was determined using the up scaled 300 mm diameter column. This data was compared to the data of the 100 mm column. Hydrodynamic characterization was performed by observing the influence of hydraulic load, rotational speed and phase ratio on DSD and φ . The total hydraulic load has a negligible influence on the DSD. The effect of varying phase ratios on the dispersed phase holdup at low hydraulic load is insignificant whereas the effect of the phase ratio at high hydraulic load has a strong impact on dispersed phase holdup. Operation experiments in pilot scale show high performance and flexibility of TCDC extraction columns. Due to the simple design of the TCDC column it is able to process highly viscous or particle laden materials and withstands harsh operation conditions. The investigation of 300mm up scaled TCDC column confirmed the scalability of the TCDC extractor design.

Kurzfassung

In dieser Masterarbeit wurde eine gerührte flüssig-flüssig Extraktionskolonne vom Typ Taylor-Couette Disc Contactor konstruiert und in Betrieb genommen. Das Kolonnendesign basiert auf den Designregeln von Aksamija [1]. Die Kolonne hat einen Durchmesser von 300 mm und eine aktive Höhe von 1 m. Für die hydrodynamischen Untersuchungen wurde die Tropfengrößenverteilung und der Holdup der dispersen Phase gemessen. Das Taylor-Couette Disc Contactor (TCDC) Design ist ein geometrisch sehr einfaches und vielversprechendes Kolonnendesign für flüssig-flüssig Extraktoren. Die hydrodynamischen Eigenschaften wurden bereits in einer kleineren Kolonne mit 100 mm Durchmesser untersucht. Die Untersuchung des um den Faktor drei vergrößerten Rührerdurchmessers, liefert Informationen über die Skalierbarkeit des TCDC Designs. Für alle durchgeführte Experimente wurde das Testsystem Wasser und ShellSol-T (Kerosin) verwendet. Wasser wird als kontinuierliche- und ShellSol-T als disperse Phase verwendet. Das TCDC Design basiert grundsätzlich auf dem Rotating Disc Contactor (RDC) Design, jedoch ohne Stator Ringe und mit vergrößertem Wellendurchmesser. Der Wellendurchmesser wurde dazu auf ein strömungstechnisch optimiertes Verhältnis von $D/d_{SH} = 0.5$ vergrößert. Dadurch werden hydrodynamische Totzonen um die Welle vermieden und das typische, als banded flow bezeichnete, Strömungsmuster eines Taylor-Couette Reaktors erzeugt. TCDC Extraktoren sind für hohe hydraulische Belastungen von mehr als $30 \text{ m}^3 \text{ m}^{-2} \text{ h}^{-1}$ geeignet. Für die Kolonnenauslegung ist eine fundierte Kenntnis über die hydrodynamischen Verhaltensweisen notwendig. Dazu wurden Daten über den Holdup der dispersen Phase (φ) und die Tropfengrößenverteilung (DSD) in der 300 mm Kolonne gesammelt und mit jenen der 100 mm Kolonne verglichen. Diese hydrodynamischen Eigenschaften wurden unter dem Aspekt des Einflusses variierender hydraulischer Belastung, unterschiedlicher Drehzahlen und Phasenverhältnisse untersucht. Es stellte sich heraus, dass die hydraulische Belastung einen vernachlässigbaren Einfluss auf die DSD hat. Ein variierendes Phasenverhältnis hat bei geringen hydraulischen Belastungen ebenfalls einen vernachlässigbaren Einfluss auf den Holdup der dispersen Phase. Im Gegensatz dazu hat ein variierendes Phasenverhältnis, bei hohen hydraulischen Belastungen, einen signifikanten Einfluss auf den Holdup der dispersen Phase. Experimente in dieser Pilotanlage bestätigen die hohe Effizienz und Flexibilität von TCDC Extraktionskolonnen. Das einfache TCDC design eignet sich bestens für viskose und stark mit Feststoffen beladene Suspensionen. Die Untersuchungen der 300 mm TCDC Kolonne bestätigen die Skalierbarkeit des TCDC Designs.

Publications

Co-author research article

2018

A. Graftschafter; , G.Rudelstorfer, M. Siebenhofer:
Hydraulics and Operation Performance of TCDC-Extractors
Chem. Ing. Tech. 2018, 90, No.6, 864-871

Contents

| | | |
|-------|---|----|
| 1 | Introduction | 1 |
| 2 | Theoretical background | 2 |
| 2.1 | Extraction | 2 |
| 2.1.1 | Liquid-Liquid extraction | 3 |
| 2.1.2 | Different types of extractors | 4 |
| 2.2 | Different types of stirred extraction columns | 5 |
| 2.2.1 | Rotating Disc Contactor - RDC | 6 |
| 2.2.2 | Taylor-Couette-Reaktor - TCR | 9 |
| 2.2.3 | Taylor-Couette Disc Contactor | 10 |
| 2.3 | Modeling of liquid-liquid extractors | 11 |
| 2.3.1 | Phase equilibrium | 11 |
| 2.3.2 | Mass Transport | 15 |
| 2.3.3 | Design of agitated liquid-liquid extraction columns | 20 |
| 2.3.4 | Design rules for the Taylor-Couette Disc Contactor | 24 |
| 3 | Design and construction | 28 |
| 3.1 | Rotor | 28 |
| 3.1.1 | Friction bearings | 30 |
| 3.2 | Column | 31 |
| 3.3 | Disperser | 31 |
| 3.4 | Peripheral devices | 32 |
| 3.4.1 | Pumps | 33 |
| 3.4.2 | Flow rate measurement | 34 |
| 3.4.3 | Gear motor and rotational speed sensor | 35 |
| 3.5 | Flowchart | 36 |
| 4 | Initial startup | 38 |
| 4.1 | Starting the column | 38 |
| 4.2 | Initial problems | 39 |
| 4.3 | Permissible operating limits | 40 |
| 5 | Experimental procedure | 41 |
| 5.1 | Dispersed phase holdup | 43 |
| 5.2 | Drop size distribution | 46 |
| 6 | Results and discussion | 50 |
| 6.1 | On-set and Flooding | 50 |
| 6.2 | Dispersed phase holdup | 51 |
| 6.3 | Sauter mean diameter and drop size distribution | 56 |
| 7 | Conclusion | 63 |
| 8 | References | 65 |
| 8.1 | References | 65 |

| | | |
|-------|--|----|
| 9 | Appendix | 68 |
| 9.1 | Symbols used | 68 |
| 9.2 | Flow sheet TCDC 300 | 71 |
| 9.3 | Hypersonic flow sensor DUK-12-G4H-F300 | 72 |
| 9.4 | Mesoscopic Probe SOPAT Pa3 | 74 |
| 9.5 | Rotational speed sensor | 75 |
| 9.5.1 | Arduino UNO program | 75 |
| 9.5.2 | Rotational speed sensor circuit | 76 |
| 9.6 | ShellSol-T technical data sheet | 77 |
| | List of Figures | 79 |
| | List of Tables | 82 |

1 Introduction

Sustainable resources are gaining more and more in importance for our society. Process intensification is the key for making bio resources usable in an economic manner. Improving and combining mass transfer unit operations for processing biobased feedstock can accelerate the economic usage of resources that actually will be burned for the purpose of generating thermal energy, resulting in a loss of residuals. The unit operation liquid-liquid extraction becomes more important due to fact that the energy demand is very low, compared to rectification processes. Highly selective solvents are available and enable extraction processes being much more effective. However, existing liquid-liquid extraction devices need to be adapted to the needs of biobased feedstock. Many devices suffer from unnecessarily complex internal design that is not suitable for highly viscous media or liquid suspensions with high amount of solid material as biobased feedstock often are. Devices show hydrodynamic dead zones along the mixing area leading to agglomeration of crud and particles, limiting the extraction efficiency. Furthermore, agglomerations can cause sudden break downs when dissolving and blocking the column. When using regular extractor designs adjustments of the internals are needed in order to perform specific separation tasks. The goal of this master thesis was to construct an agitated liquid-liquid counter current extraction column with 300mm column diameter and take it in operation as well as investigate its properties. The rotor design is based on the design rules and publications of Aksamija [1] and Graftschafter et al. [2]. The Taylor-Cuette Disc Contactor (TCDC) is a hybrid design between the Rotating Disc Contactor (RDC) and Taylor-Couette reactor (TCR). Simplification of the RDC design allows the construction of an apparatus without hydraulic dead zones that can handle highly viscous liquid suspensions with high amounts of solid material. Using the TCDC design enables a reduction of material costs and expensive downtimes. Downtimes are reduced by the fact that this design is insensitive to any kind of crud and agglomerations. The combination of reaction and extraction in one continuous process becomes possible by adding solid material (e.g. solid catalyst) to the binary liquid system. The first part of this thesis is about theoretical background explaining the reactor design and basic mass transfer theory. The second part is about constructing and taking the TCDC 300 mm column into operation. In the experimental part the drop size distribution (DSD) and dispersed phase holdup is measured at different rotational speeds and varying hydraulic loads. The experimental data is compared to already existing data from the TCDC 100 mm column. Existing empiric correlations for predictions of holdup and the Sauter mean diameter are compared to the experimental result. This should show feasibility for the scale up the TCDC liquid-liquid extractor design.

2 Theoretical background

This thesis is about liquid-liquid extraction in a stirred extraction column called Taylor-Couette Disc Contactor (TCDC). In the first chapter the basic working principles of liquid-liquid extraction are explained. Furthermore, the working principles and design rules of several stirred liquid-liquid extraction columns are explained in more detail.

2.1 Extraction

In general extraction is defined as selective transport of a valuable substance from a carrier phase to a solvent phase caused by different solubility. To perform extraction successfully, it is essential that the solvent phase and the carrier phase are not miscible and exhibit a wide miscibility gap. After the extraction process the product (or valuable substance) is dissolved into the solvent phase. In distinction from other separation processes the product does not show up as a pure substance and needs further separation steps. Rectification is often used as subsequent separation of the product substance from the solvent phase. In many industrial applications the solvent phase is regenerated after extraction and is used again as recycled solvent. The raffinate remains with a very low concentration of the valuable substance. Following forms of extractions can be distinguished: [3].

- Solid-liquid extraction (washing, leaching)
- Liquid-liquid extraction
- High pressure extraction (supercritical or liquid state)
- Gas-liquid extraction (absorption)

Selecting the right solvent is the most essential step for all extraction processes. Several guidelines are available that can be used for finding the most suitable solvent. The solvent must comply with the following requirements: high selectivity of the key component and developed miscible gap to the carrier phase. Selectivity describes the property to dissolve only one component of the material system. With an increasing amount of components in a system the amount of unwanted substances in the loaded solvent increases. Since binary systems are rare in reality it is much more important to choose the right solvent for the extraction process. Biobased feedstock for example contain a number of different substances. The goal is to find a solvent that is highly selective for the specific key component [4].

The basic operation process for extraction is shown in Figure 2-1. The treated liquid labels the raffinate outlet stream. The loaded solvent (extract) has to be separated from the key substance and recycled before it can be used again.

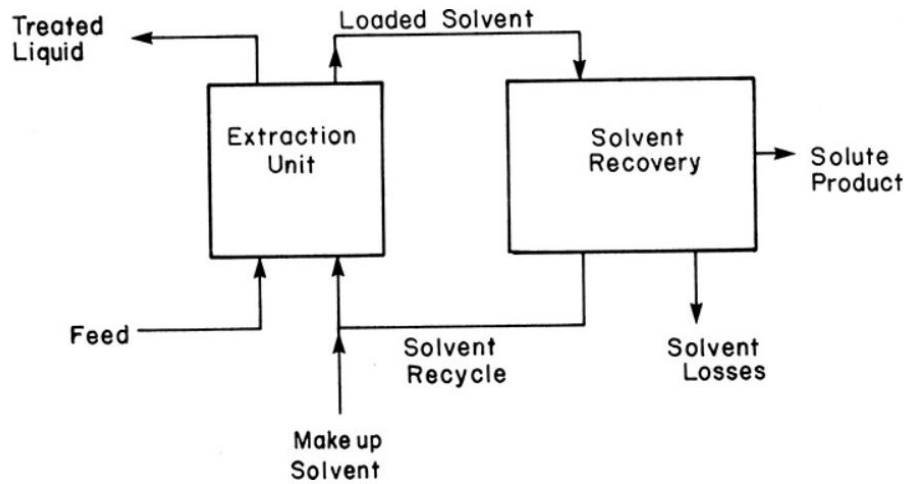


Fig. 2-1: Basic extraction process including solvent regeneration [5]

2.1.1 Liquid-Liquid extraction

Liquid-liquid extraction gains more and more in importance because of its low energy consumption compared to rectification process. There are several reasons why liquid-liquid extraction is preferred to other separation processes. [3]

- The components are thermally sensitive or tend to react at high temperatures
- The mixture has a very high or low boiling point so rectification becomes uneconomic (additional energy is necessary)
- The boiling points of the components are similar or form an azeotrope
- Several substances with a wide range of boiling points should be separated at once
- The concentration of the key component is very low and distillation becomes very expensive

Liquid-liquid extraction requires different densities of the immiscible fluids to allow easy and fast separation after contact. Mass transfer is mainly influenced by the following parameters: holdup of dispersed phase, mass transfer coefficient, specific area for mass transfer and concentration gradient. The main goal of liquid-liquid extraction is to maximize mass transfer and thus the separation efficiency. Mass transfer is limited by the equilibrium and supported by degree of mixing and contact

area between the dispersed and continuous phase. High turbulence and high relative velocities between the two phases increase the mass transfer coefficient. The main driving force of every mass transfer operation is the concentration gradient. This concentration gradient decreases with increasing axial backmixing in continuous extraction devices. Especially in continuously stirred liquid-liquid extractors the axial backmixing can not be neglected. Many extraction devices thus use special internals to decrease the influence of axial backmixing. In the next section some different extraction devices are described. [6]

2.1.2 Different types of extractors

Over the last decades many different types of extraction columns were developed. Energy input can increase the mass transfer area and contact time of the two phases. The additional energy can be added by e.g. pulsation, stirring or centrifugation. Figure 2-2 shows a possible way for the characterization of extraction devices. The TCDC extraction column is classified as a column with rotating internals (mixer) as marked in figure 2-2. With the additional energy input the contact time and drop size distribution of the dispersed phase can be adjusted. Without additional energy input the drop size distribution is determined by the potential energy of the dispersed phase in the liquid system. This kind of droplet formation can be observed in a sieve tray column. This mostly big and fast ascending droplets decrease the efficiency of the extraction column. Big droplets decrease the available area for mass transfer and fast ascending droplets have too little time to reach equilibrium state. This happens due to non-ideal mixing inside the droplet combined with poor interface renewal. This decreases the concentration coefficient. Static columns can suffer from poor mass transfer caused by unfavorable drop size distribution and low dispersed phase holdup due to free ascending droplets.

Counter current extraction devices without energy input are only used if the number of separation stages is low [3]. Packed columns or sieve tray columns can be named as examples for representative devices without energy input. These devices are well probed and construction algorithms are available. However, additional energy input by stirring increases the dispersed phase hold up by decreasing the droplet size and homogenizes the drop size distribution in the system. These additional parameters are used to optimize the mass transfer in the specific column [3].

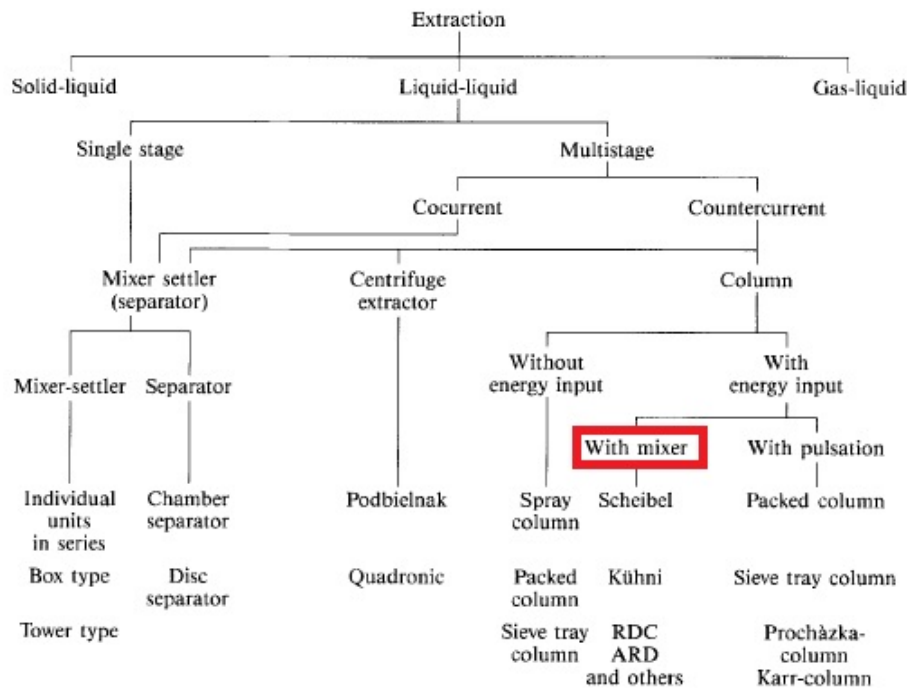


Fig. 2-2: Overview of extraction operations and extractor designs. The red margin shows the focus of this thesis [3]

2.2 Different types of stirred extraction columns

There are several geometric designs of stirred liquid-liquid extraction columns available on the market, most of them operating in counter current mode. With the stirrer's rate of rotation, droplet size distribution and the amount of dispersed phase holdup can be effected. Increasing shear forces at the stirrer decreases droplet size and thus increases the dispersed phase holdup. The maximum rotational speed is limited by the flooding point of the column. If the vorticity of the continuous phase overcomes the buoyancy of the dispersed phase, the column gets blocked. At very high rotational speeds the droplet size of the dispersed phase decreases to a point where an emulsion is formed where the columns get blocked as well. The flooding also depends on the volumetric flow rates of the liquid phases. At high volumetric flow rates flooding occurs at lower rotational speed compared to low volumetric flow rates. The efficiency of stirred extraction columns is decreased by the effect of axial backmixing. The concentration gradient decreases due to axial backmixing. The negative effect of axial backmixing can be reduced by static internals that prevent rising droplets from being forced back in the column. Forced back droplets decrease the concentration gradient at the actual height in the column. The RDC design uses stator rings to divide the column into individual compartments to inhibit backmixing. These static internals decrease possible volumetric throughput and give place for hydrodynamic

dead zones. With increasing complexity of static internals the free cross sectional area and possible total hydraulic load decrease. The challenge is to find the optimum between:

- High hydraulic load [$m^3m^{-2}h^{-1}$]
- High dispersed phase holdup
- High residence time of the dispersed phase and the continuous phase [s]
- Low axial backmixing [m^2s^{-1}]
- Optimized geometric design to avoid hydrodynamic dead zones

Hydrodynamic dead zones tend to form agglomerations of crud and thus can decrease the separation efficiency of the column. Therefore it is important to avoid hydrodynamic dead zones along the active mixing zone. After intensive phase contact the column has to provide sufficient settler area for coalescing. The cross sectional area of the settler zone influences the time for this sedimentation process.

Two commonly used geometric designs of stirred liquid-liquid extraction columns are shown in figure 2-3. Figure a shows a Kühni column and in figure b a Rotating Disc Contactor is shown. For instance the company *Sulzer* sells these two different geometric designs of liquid liquid extractors. For an industrial scale up of these columns, literature does not provide information about a suitable scale up of the rotor shaft. Many industrial applications show too small rotor shaft diameters and thus hydrodynamic dead zones can arise at the area of the rotor shaft. In this case the dispersed phase accumulates around the area of the shaft and thus proper phase contact is missing. A complex design of internals is often very expensive and tends to form hydrodynamic dead zones located at the edges between stator and wall. However these types of extraction columns are well investigated and recommendations for column design are available. This thesis investigates a hybrid design between RDC and TCR extraction columns. In the following section these designs are explained in more detail. [1, 3, 6]

2.2.1 Rotating Disc Contactor - RDC

The working principle of the Rotating Disc Contactor (RDC) is shown in figure 2-3 b. The rotor discs are mounted on the spinning shaft. Stator rings are fixed on the outer area of the column and are used to prevent high axial backmixing. The heavier phase is added at the top of the column and the light phase at the bottom. Due to the spinning

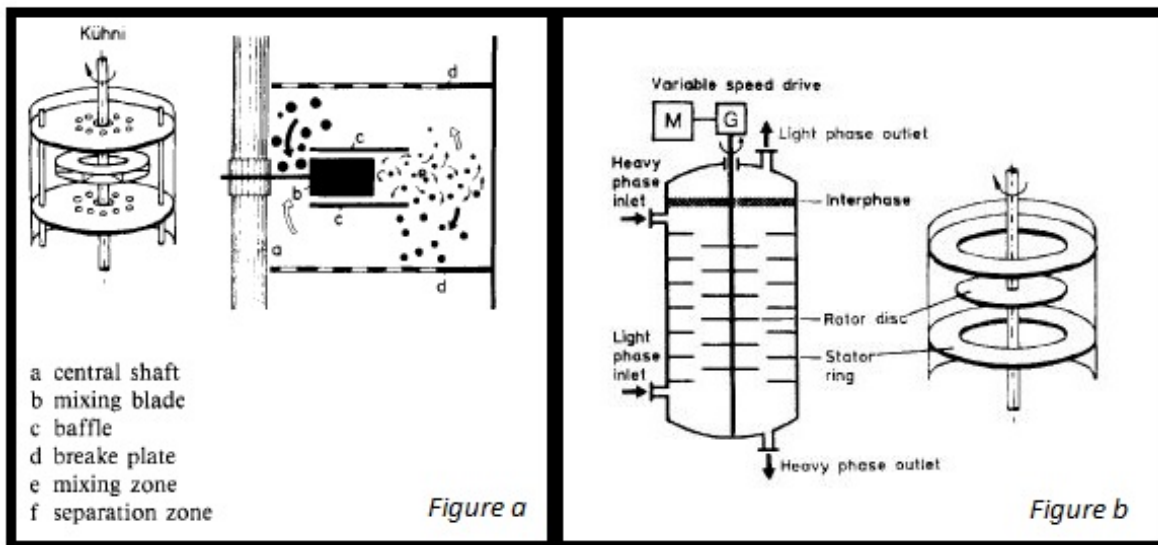


Fig. 2-3: Figure (a) shows a "Kühni" column and figure (b) shows a Rotating Disc Contactor (RDC). Both designs use static internals to separate the column into compartments and to avoid backmixing. [3]

rotor discs two toroidal vortexes in each compartment (area between two stator rings) are formed. These vortexes are shown in figure 2-4. Inside the compartment the liquids are well mixed and due to counter current flow high separation efficiency is possible. Column diameters up to 8 meters are possible. A maximum hydraulic load up to $40 \text{ m}^3 \text{ m}^{-2} \text{ h}^{-1}$ can be realized, which is one of the main benefits of the RDC [3]. Due to the variation of the rotor speed it is possible to adjust the droplet size and simplify dispersion of highly viscous liquids. In literature many different designs for internals can be found. These internals aim to minimize axial backmixing and thus improving the height of theoretical separation units. The significant improvement of separation efficiency due to static internals often decrease the maximal volumetric flow rates. The main advantages of the RDC are the high hydraulic load and the simple design of internals, compared to other extraction columns. Design of extraction columns requires certain knowledge about the specific mass transfer area. The available mass transfer area can be calculated with the Sauter mean diameter and the dispersed phase holdup. The axial dispersion coefficient considers the decreasing efficiency due to the effect of axial backmixing. The Sauter mean diameter can be predicted using correlations shown in table 2-1. Correlations to predict the dispersed phase holdup and axial dispersion coefficients for standard RDC columns are collected by Grafschafter et al. [2].

Tab. 2-1: Empirical correlations for predicting the mean Sauter diameter in RDC columns including geometric specifications

| Correlation | Author | System properties | Geometry [m] |
|--|------------------------|--|-------------------|
| $d_{32} = 16.7 \left(\frac{\sigma}{\rho_c g} \right)^{0.5} \left(\frac{D_R n \rho_c}{\eta_c} \right)^{-0.3} \left(\frac{n^2 D_R}{g} \right) N_C^{-0.23}$ | Kagan [7] | $\rho_c = 1000 - 1230 \left[\frac{\text{kg}}{\text{m}^3} \right]$ $\rho_D = 725 - 1430 \left[\frac{\text{kg}}{\text{m}^3} \right]$ $\eta_C = 1 - 2.5 \text{ [mPa s]}$ $\eta_D = 0.3 - 48 \text{ [mPa s]}$ $\sigma = 13 - 38.5 \left[\frac{\text{mN}}{\text{m}} \right]$ | $D = 0.054 - 0.2$ |
| $d_{32} = 0.62 \frac{D_R}{W_R^{0.52}} \left(1 + \frac{35}{N_C^{1.22} W_g^{0.5}} \right) (1 + 2\varphi)$ | Fischer [8] | $\rho_c \approx 1000 \left[\frac{\text{kg}}{\text{m}^3} \right]$ $\Delta\rho = 95 - 335 \left[\frac{\text{kg}}{\text{m}^3} \right]$ $\eta_C = 1 - 4.8 \text{ [mPa s]}$ $\sigma = 12 - 44.5 \left[\frac{\text{mN}}{\text{m}} \right]$ | $D = 0.150$ |
| $We = \frac{n^2 D_R^3 \rho_c}{\sigma}$ | | | |
| $\frac{d_{32}}{D_R} = \frac{C_1}{0.07 + \sqrt{Fr_R}} \left(\frac{\eta_c}{\sqrt{\sigma \rho_c D_R}} \right)^{-0.12} \left(\frac{\rho_d}{\rho_c} \right)^{0.16} \left(\frac{D_R^2 \rho_c g}{\sigma} \right)^{-0.59} \left(\frac{H_C}{D} \right)^{0.25} \left(\frac{D}{D_R} \right)^{0.46}$ $\left(\frac{D_R^2 \rho_c g}{\sigma} \right)^{-0.59} \left(\frac{H_C}{D} \right)^{0.25} \left(\frac{D}{D_R} \right)^{0.46}$ $Fr_R = \frac{n^2 D_R}{g}$ $C_1 = 0.53$ | Kumar and Hartland [9] | | |
| $n = \frac{0.374^{0.667}}{D_R^{0.778} (\rho_c)^{0.332} d_{32}^{0.566}}$ | Marr[10] | | |

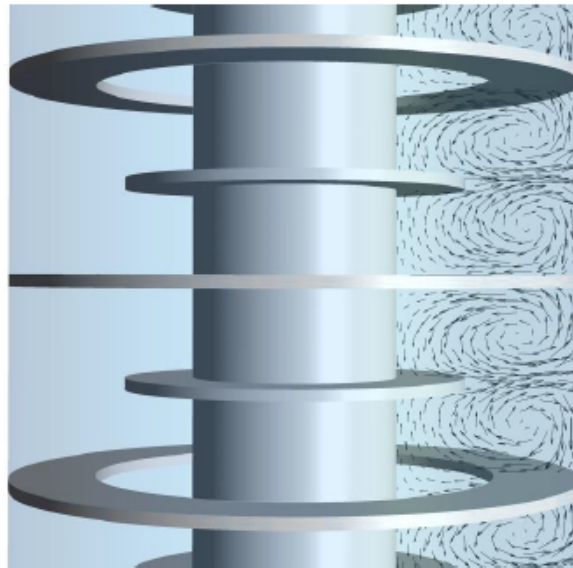


Fig. 2-4: Toroidal vortex formation in a RDC Column [1]

2.2.2 Taylor-Couette-Reaktor - TCR

The Taylor-Couette systems is explained to understand the formation of toroidal vortices formation in a Taylor-Couette reactor. Couette flow can be described by laminar flow that is formed between two parallel plane plates whereby one of the planes is moved in one direction and forms the flow profile $u_{(x)}$ as shown in the left figure 2-5. The shear rate $\dot{\gamma}$ remains constant over the gap between the two plates (equation 2-1). The left figure 2-5 shows the plane Couette-flow. The right figure 2-5 shows cylindrical Couette flow between two concentric cylinders whereby the outer cylinder is rotating. Cylindrical Couette flow can be used to measure viscosity of fluids. In Taylor-Couette reactors (TCR) the benefits of Taylor vortices are used. Taylor vortices occur after the cylinders have reached a critical rotational speed that depends on liquid properties and diameter of the cylinders. Due to the possibility of both cylinders being able to be turned independently from each other, many different flow patterns are possible. [11]

$$\dot{\gamma} = \frac{U}{d} \quad (2-1)$$

Basic TCRs consist of two concentric cylinders with one rotating cylinder. The other cylinder remains motionless. Andereck et al. [11] gives an overview about possible flow regimes. Such flow regimes are for instance: corkscrew-flow, wavy vortex-flow or turbulent Taylor vortices. Figure 2-6 shows the toroidal vortices caused by an inner spinning cylinder. As mentioned above, these vortices are called Taylor-vortices. A

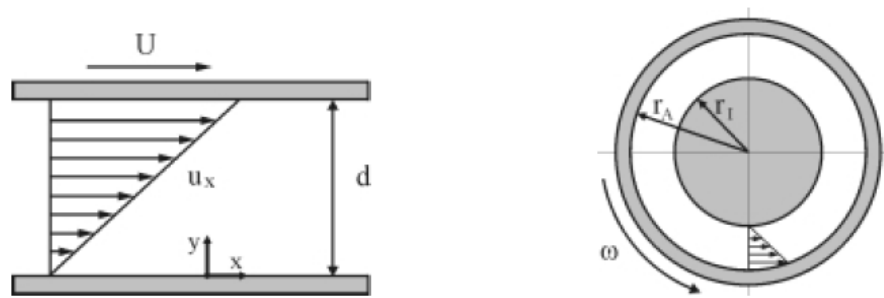


Fig. 2-5: left: plane Couette flow; right: cylindrical Couette flow [12]

Taylor-vortex is stable if the centrifugal force is higher than the counteractive force from the viscosity of the fluid. The centrifugal force of the inner cylinder centrifuges the fluid against the outer cylinder and due to conservation of momentum and mass axisymmetric toroidal vortices are formed. This is known as Taylor vortex flow. [11, 13, 12]

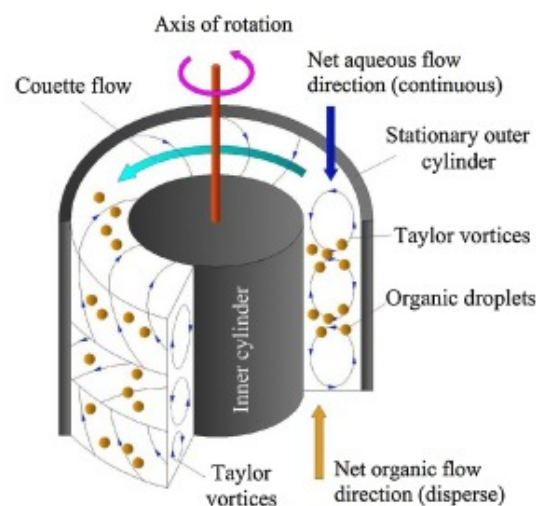


Fig. 2-6: Taylor-Couette flow in a TCR [13]

2.2.3 Taylor-Couette Disc Contactor

In the year 2014 Aksamija [1] showed that as a result of CFD simulations and experimental validation, combining the hydrodynamic behavior of RDC and TCR leads to a new simplified design of internals with stable flow regime, no hydrodynamic dead zones and equal separation efficiency. Compared to the RDC the TCDC design does not require stator rings to stabilize the flow regime. Increased rotor disc diameter and shaft diameter lead to a optimized design without hydrodynamic dead zones. The increased rotor discs stabilize the banded two phase flow pattern that is formed due to

the increased shaft diameter. Banded two phase flow also occurs in a Taylor-Couette system. In addition the increased rotor disc diameter prevents high axial backmixing. Due to the simplified design less material is needed and dead zones for crud agglomeration are avoided. Figure 2-7 shows the toroidal vortices from CFD simulations inside a single compartment. The left figure shows the flow pattern of the RDC and the right figure shows the optimized TCDC column design without stator rings and increased rotor disc diameter and shaft diameter. [1, 2]

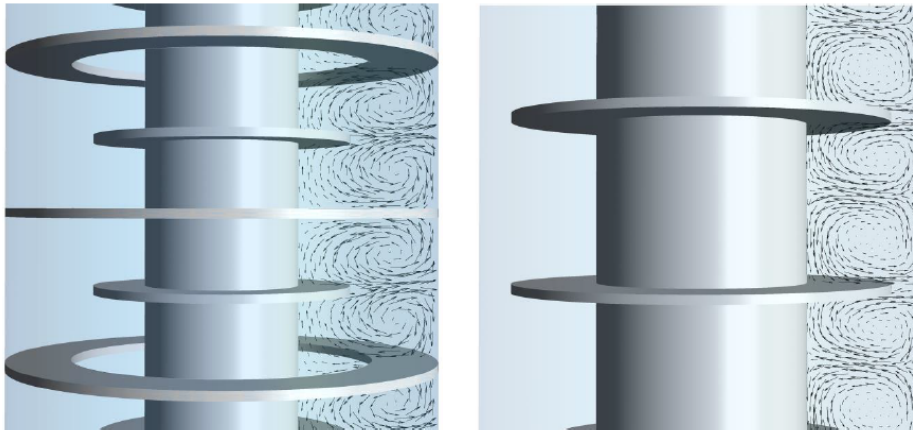


Fig. 2-7: left: flow pattern in a RDC column; right: flow pattern in a TCDC column [1]

2.3 Modeling of liquid-liquid extractors

Liquid-liquid extraction is defined as mass transfer from one fluid to another. For understanding the complex operation that occurs in a agitated extraction column it is necessary to have certain knowledge of the phase equilibrium in the ternary system and to understand the hydrodynamic behavior of the column. The driving force for mass transfer of component A is the concentration gradient (Δc_A) between the feed and the solvent. The system pursues to a thermodynamic balanced state. In this section the basic mass transfer process in a liquid-liquid extractor is explained and design correlations for TCDC columns are defined.

2.3.1 Phase equilibrium

Each system is forced to reach equilibrium state. Separation processes change the concentration of a certain component. Equilibrium state can be distinguished between mechanical equilibria, thermal equilibria and diffusive equilibria. A mechanically balanced system has the same pressure, a thermally balanced system the same temperature and a diffusive balanced system has equal chemical potentials. Equilibrium

is reached when all thermodynamic potentials are at a minimum [3]. Equation 2-3 to 2-4 express equilibrium state for a given binary system.

$$p^\alpha = p^\beta \rightarrow dp = 0 \quad (2-2)$$

$$T^\alpha = T^\beta \rightarrow dT = 0 \quad (2-3)$$

$$\mu_i^\alpha = \mu_i^\beta \rightarrow d\mu_i = 0 \quad (2-4)$$

The first law of thermodynamics (equation 2-5) states that energy can neither be created nor destroyed in an isolated system. Energy can only be transferred or changed from one form to another. The inner Energy U is defined as the energy that can be exchanged to environment due to work W or thermal energy ΔQ .

$$dU = dQ + dW \quad (2-5)$$

Since the first law of thermodynamics cannot describe irreversible processes the first law is extended to the second law of thermodynamics by defining the entropy S . The entropy S is used to express the direction of energy conversion. Every system aspires to a maximum entropy and thus a minimum inner energy U (equation 2-6).

$$dU = T * dS - p * dV \quad (2-6)$$

The equilibrium state is reached if the internal energy reaches a minimum and entropy reaches a maximum. But this definition gives no information about the chemical compensation process happening due to mixing operations, matter exchange or conversion and compensating transactions in a system. For the description of these transactions *Gibbs* the chemical potential 2-7 is added to the second thermodynamic law.

$$dU = T * dS - p * dV + \sum \mu_i * dn_i \quad (2-7)$$

The chemical potential is the driving force for chemical reactions, diffusive mass transfer and phase change. The chemical potential (equation 2-8) is defined as the partial molar derivation of Gibbs-energy G to the amount of substance. This is called the partial molar Gibbs energy.

$$\mu_i(T, p, x) = \left(\frac{\partial G}{\partial n_i} \right)_{T, p, n_j} \quad (2-8)$$

Gibbs energy can also be described by using the fugacity f (equation: 2-9).

$$dG = R * T * d(\ln f) \quad (2-9)$$

Fugacity is an auxiliary variable to simplify the definition of the chemical potential. So the equilibrium state can be defined by fugacity as follows: 2-10.

$$f_i^\alpha = f_i^\beta \rightarrow df_i = 0 \quad (2-10)$$

For liquid-liquid extraction it is necessary that the two phases show a distinct miscibility gap. A homogeneous liquid mixture separates in two phases if the mixed phase is not stable. A stable condition is defined as a minimal state of free enthalpy in the system. Free molar mixing enthalpy is called molar Gibbs energy. The system is defined as unstable if the molar free enthalpy has a maximum and two turning points. Curve b in figure 2-8 show a miscibility gap between C1 and C2. Between the two turning points W1 and W2 the mixture is unstable. A tiny interruption can separate the mixture into two stable phases. Between the two turning points the curve matches the instability criteria as defined in equation 2-11. [14]

$$\left(\frac{\partial^2 \bar{G}}{\partial x^2}\right)_{T,p} < 0 \quad (2-11)$$

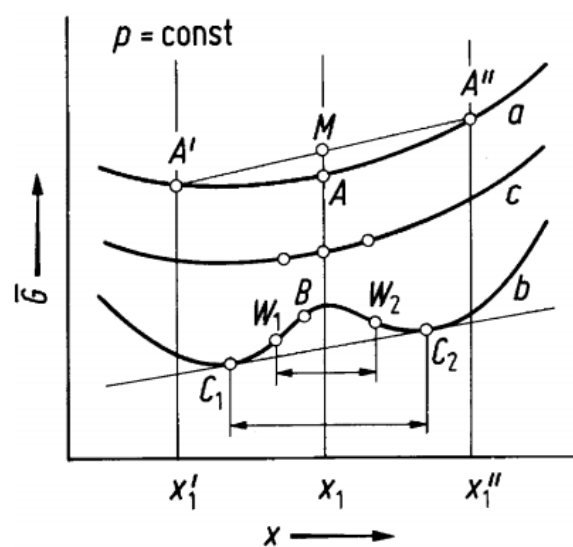


Fig. 2-8: Molar free mixing enthalpy gives information about stability of binary mixtures: curve (a), stable mixture; curve (b), turning points get closer and define the critical separation point; curve (c), unstable system between W_1 and W_1 the miscibility gap is located between C_1 and C_2 [14]

For liquid-liquid extraction the triangle diagram is an important tool to visualize the extraction process of a ternary system. This diagram includes information about the miscibility gap. At the edges of the diagram the pure substances are denoted. The binodal curve defines the two-phase area from the single-phase area. Above the binodal (\overline{CPD}) curve, as shown in figure 2-9, the ternary mixture exists as one homogeneous phase. Below the binodal curve the phase equilibrium and thus a minimal amount of free enthalpy is reached [3]. At this state two coexisting phases are present. The binodal curve can be determined by experiments. An immiscible solvent is added to a mixture containing key component A. The two phases are extracted from a separating funnel and after segregation the concentrations of key component A are measured on both phases. These concentrations are points on the binodal curve. The connection between these two points is called tie line (\overline{CD}). Tie lines give information about the equilibrium distribution of key component A in the two phases. Increasing the slope of the tie lines increases separation efficiency of one extraction step. Distribution of key component A in the two phases is defined by Nernst Partition law. The triangular diagram can be used to get information about the extraction effort. Number of extraction stages can be estimated. [3]

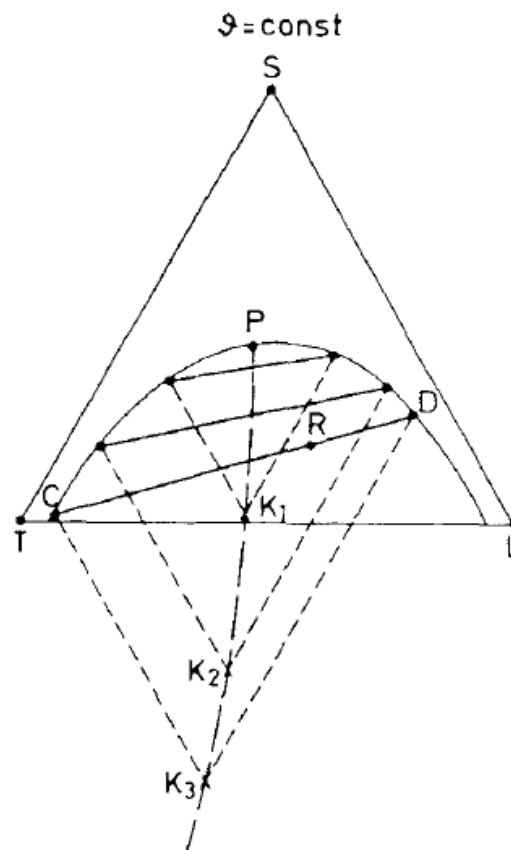


Fig. 2-9: Triangular diagram with two phase area. Below the binodal curve (\overline{CPD}) the mixture separates into two stable phases. Above the binodal curve the ternary mixture exists as one homogeneous phase. (\overline{CD}) is called tie line and defines the distribution of key component A in the two phases. [3]

2.3.2 Mass Transport

Mass transfer is defined as substance transport in the phase to the phase boundary. The mass transfer coefficient β [$m s^{-1}$] is used to calculate the transferred amount of a specific substance to the phase boundary. For very simple flow regimes like laminar flow analytical solutions to calculate the mass transfer coefficient are possible. Complex turbulent flow regimes require different mass transfer theories for the determination of β . The concentration gradient Δc_a of a substance A is the driving force for mass transfer operations. Every thermodynamic system aims to reach equilibrium state. This equilibrium state is reached if the concentration of key component A hits

the binodal curve. Equation 2-12 describes the basic mass transfer from the bulk to the boundary layer.

$$\dot{n}_A = \frac{\dot{N}_A}{A} = \beta * \Delta c_A \quad (2-12)$$

Models and empirical correlations are used to get information about β . The dimensionless Sherwood number represents the mass transfer coefficient. In equation 2-13 L is the characteristic length and $D [m^2s^{-1}]$ is defined as dispersion coefficient. For simple flow regimes like laminar flow over a plate analytic solutions for Sh are possible. [3]

$$Sh = \frac{\beta * L}{D} \quad (2-13)$$

In practice real flow patterns are very complex. Following theories can be used to determine the Sherwood number.

- **Film theory:**

The film theory is the easiest and oldest model. This theory assumes that mass transfer occurs in a very small film near to the phase boundary. At the phase boundary layer equilibrium state is given. Figure 2-10 shows a schematic drawing of the film theory approach. Component A is transferred to a fluid b. The bulk velocity $w_{w,\infty}$ and bulk concentration $c_{A,\infty}$ remain constant. Mass transfer only takes place in the thin boundary layer. The velocity boundary layer δ_w is much thicker than the concentration boundary layer δ_c . Concentration and velocity only change in y direction. Therefore the velocity boundary layer is much thicker than the concentration boundary layer. The velocity in the concentration boundary layer is very low. These conditions are mostly given if the Schmidt number (Sc) is bigger than 1. In this case mass transfer at the phase boundary is performed by molecular diffusion. At stationary flow the material flow density remains constant in time in y direction (equation 2-15).

$$\frac{d\dot{n}_A}{dy} = 0 \quad (2-14)$$

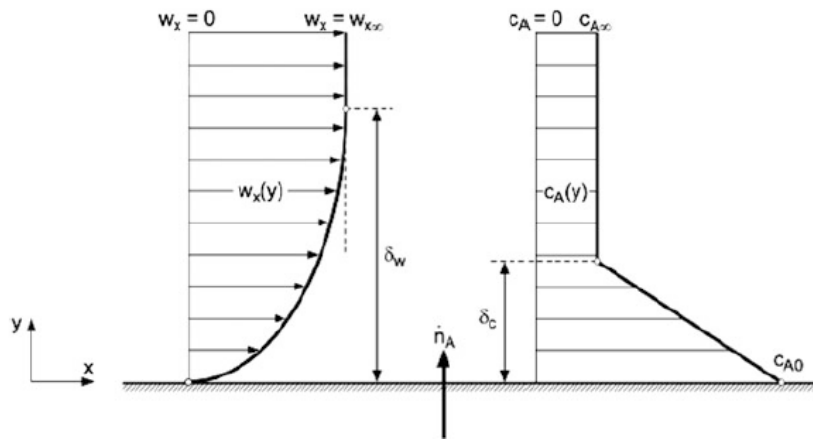


Fig. 2-10: Concentration and velocity profile for laminar flow on a plane plate according to the film theory. [15]

The mass transfer coefficient can be calculated according to equation 2-15. In this equation the thickness of the concentration boundary layer δ_c is unknown. Literature recommends application-oriented empirical correlations to estimate the thickness of concentration boundary layer.

$$\beta = \frac{D}{\delta_c} \quad (2-15)$$

• Boundary layer theory

The boundary layer theory assumes that mass transfer is also only performed in the small boundary layer. In contrast to the film theory, concentration and velocity can change in x and y direction, whereby convective mass transfer than be considered. The differential equation is simplified by using the average mass transfer coefficient β_L over the length. In most technical applications this simplification is sufficient. The equation 2-16 defines the average mass transfer coefficient over the length in z direction.

$$\beta_L = \frac{1}{L} * \int_{z=0}^L \beta * dz \quad (2-16)$$

The average mass transfer coefficient can be calculated using the Sherwood approach according to equation 2-17. The average Sherwood number is described as a function of the Reynolds- and the Schmidt number. Depending on the flow, different potential approaches are available. These approaches can

be used for easy geometries. An overview of the potential approaches can be found in *Transportvorgänge in der Verfahrenstechnik* [15].

$$Sh_L = \frac{\beta_L * L}{D} = f(Re, Sc) \quad (2-17)$$

- **Penetration and surface renewal theory**

The film- and boundary layer theory assumes stationary mass transport. Penetration theory take into account that fluid droplets or particles have a short contact time with the phase boundary layer and thus equilibrium can not be reached. The Fluid element has a defined contact time τ at the boundary layer. After this time this fluid element leaves the boundary layer and is mixed in with the bulk. A fluid element is replaced by a new element after a defined contact time. This is called surface renewal theory. This theory considers the varying contact times and maps them in a residence time distribution. The equation 2-18 is used to calculate the mass transfer coefficient β considering the contact time. [15]

$$\beta = \frac{2}{\sqrt{\pi}} \sqrt{\frac{D}{\tau}} \quad (2-18)$$

- **Theory of turbulence**

For the quantitative description of turbulent mass transfer average mass transfer coefficients are used. Turbulent mass transfer is practically performed in every real apparatus. The turbulent mass transfer coefficient cannot be calculated because it depends on the kind of turbulence and all theories mentioned before use simplifications like laminar flow or stationary mass transfer. [15]

- **Overall mass transfer: Two Film Theory**

Overall mass transfer can be described by the two film theory. In this theory overall mass transfer occurs between two adjoining phases. Equilibrium state is assumed at the phase boundary layer and only mass transport by molecular diffusion without resistance takes place [3]. On the other hand mass transfer in the bulk phase is very fast due to turbulent flow. The equilibrium state at the interface is defined to equation 2-19 where K^* is the dimensionless phase equilibrium constant. Figure 2-11 illustrates the following definitions.

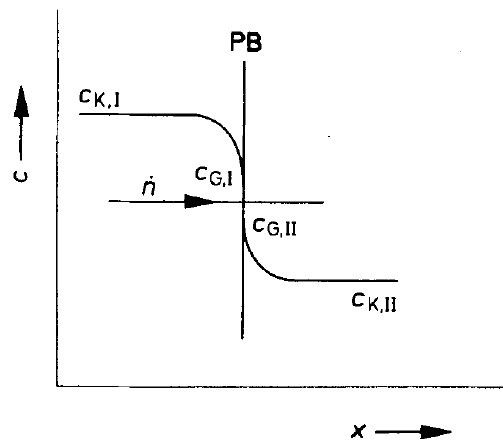


Fig. 2-11: Mass transition according to two film theory: PB defines the phase boundary layer, c_k is the concentration in the bulk and c_g is the concentration at the phase boundary layer [3]

$$c_{G,I} = K^* c_{G,II} \quad (2-19)$$

$$c_{K,I} - c_{G,I} = \frac{\dot{N}}{\beta_I A} \quad (2-20)$$

$$c_{G,II} - c_{K,II} = \frac{\dot{N}}{\beta_{II} A} \quad (2-21)$$

The mass transfer coefficient has to be referred to one phase. One component of phase I is transmitted into phase II. The over all mass transfer coefficient can be calculated using the mass transfer coefficients shown in equation 2-23 or 2-25. If the key component A is transferred from fluid I to fluid II the transferred amount of component A can be calculated according to equation 2-22 or 2-24, where c^* defines equilibrium concentration. The concentrations $c_{G,I}$ and $c_{G,II}$ in the phase boundary layer can not be measured. To eliminate these concentrations the mass transport coefficients, k_I and k_{II} are introduced. If $\beta_{II} \gg \beta_I$ then $k_I \approx \beta_I$ or the other way round. In this case the over all mass transport resistance is primary located at phase I or II. This is the reason why β_I and β_{II} can differ up

to the power of ten. The mass transfer coefficient β_{II} in the continuous phase can be calculated with empirical correlations.

$$\dot{N} = k_{II} * A * (c_{II}^* - c_{K,II}) \quad (2-22)$$

$$\dot{N} = k_I * A * (c_{K,I} - c_I^*) \quad (2-23)$$

$$\frac{1}{k_{II}} = \frac{1}{\beta_{II}} + \frac{1}{K^* * \beta_I} \quad (2-24)$$

$$\frac{1}{k_I} = \frac{1}{\beta_I} + \frac{K^*}{\beta_{II}} \quad (2-25)$$

A in equation 2-22 and 2-23 is defined as the available area for mass transport. For instance in liquid-liquid extraction the whole area of all rising droplets has to be considered. The specific mass transfer area (a) can be calculated with the Sauter mean diameter (d_{32}) and the dispersed phase holdup (φ), as shown in equation 2-27. The total area for mass transfer is calculated by multiplying the specific area (a) with the liquid reactor volume (equation 2-26). ψ defines the sphericity of the droplets. For instance if $\psi = 1$ the droplets are assumed as rigid spheres.

$$A = a_v * V_{Reactor} \quad (2-26)$$

$$a_v = 6 * \frac{\varphi}{d_{32}} * \psi \quad (2-27)$$

2.3.3 Design of agitated liquid-liquid extraction columns

In the previous section basic information about mass transfer was given. Stirred extraction columns suffer from distinct axial backmixing. Axial backmixing reduces mass transfer due to a decreased concentration gradient. Calculation and estimation of mass transfer coefficient in liquid-liquid extraction columns is very difficult. Turbulent flow regime in columns entails significant axial backmixing. Figure 2-12 illustrates the effect of axial backmixing on the separation efficiency of extraction columns. In this figure, \overline{EC} denotes the equilibrium line of the system. The theoretical operation line when assuming plug flow is denoted as \overline{BL} . For comparison the operation line \overline{OL} obtained for pronounced axial backmixing is also shown in this figure. The number of theoretical stages for \overline{OL} is higher than for \overline{BL} due to axial backmixing. This in turn leads to an increase of column height needed to reach the required concentrations in

the extract and the raffinate. X defines molar loading in the raffinate phase and Y the molar loading into the extract phase both referring to the key component. [3, 15]

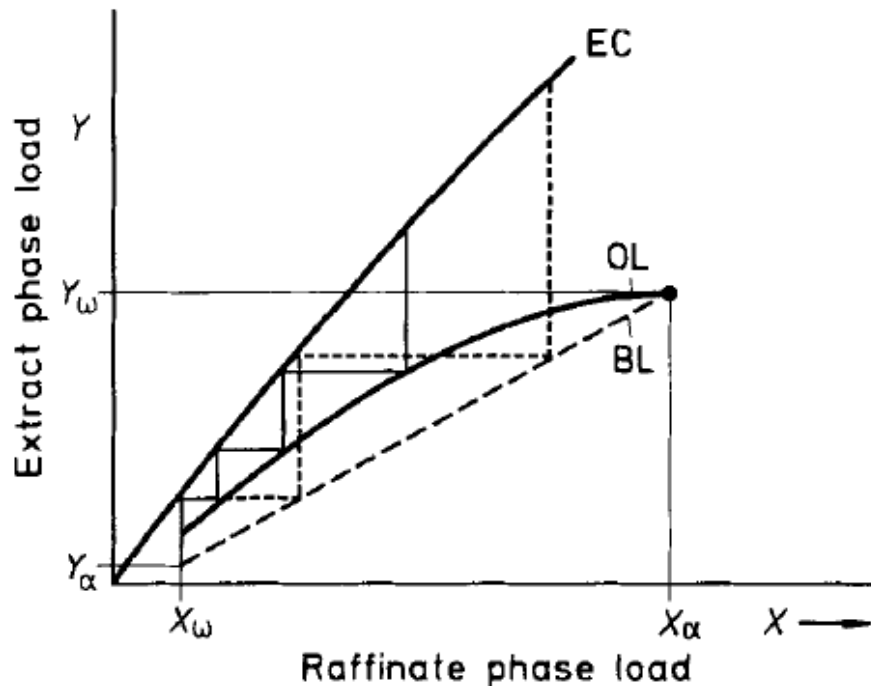


Fig. 2-12: Influence of axial backmixing on theoretical separation units and balance line (BL). EC defines the equilibrium line and OL defines the operation line. [3]

Dispersion model

Information about axial backmixing in extraction columns is necessary for column design. Empirical correlations are available for the prediction of axial backmixing coefficients. Axial backmixing of the continuous phase can for example be determined by measuring the residence time by adding a tracer substance to the feed of the continuous phase. In this case it is important that the tracer substance used is inert to the component system used. Tracer substances are for example electrolytes, dyes or radioactive materials. Measuring the electric conductivity is a simple way to determine axial backmixing. Figure 2-13 shows the change of the tracer signal along the extractor length. With this data the axial dispersion coefficient D_{ax} can be calculated by applying the dispersion model. The axial dispersion coefficient is used to describe the effect of backmixing in the HTU-NTU concept. [16] The real flow pattern in the column deviates from ideal plug flow. This deviation can be described using the dispersion model. The dispersion model describes the real flow pattern as

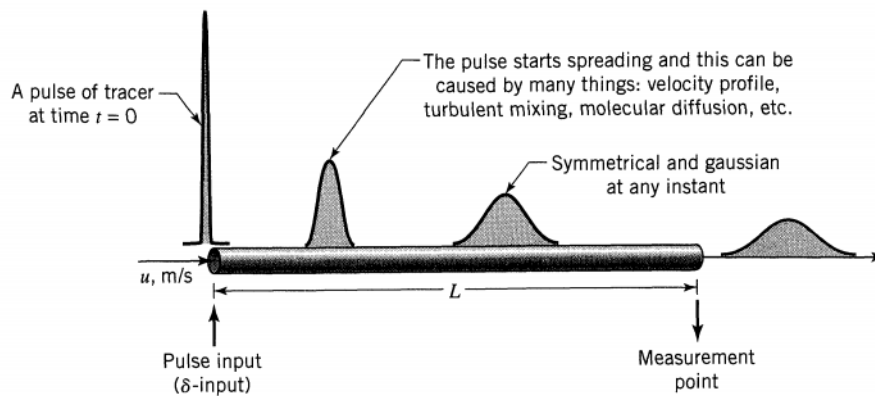


Fig. 2-13: Tracer signal to measure axial back mixing [16]

combination of dispersive and convective transport. The axial dispersion coefficient D_{ax} has the same dimension as the diffusion coefficient. Dispersion is defined by the second Fick'sch law as shown in equation 2-28.

$$\frac{\partial c}{\partial t} = D \frac{\partial^2 c}{\partial x^2} \quad (2-28)$$

Figure 2-14 shows the two transport terms of convective and dispersive transport. The combination of these transport terms leads to equation 2-29. \bar{v} defines the superficial face velocity for the convective term.

$$\frac{\partial c}{\partial t} = D_{ax} * \frac{\partial^2 c}{\partial x^2} - \bar{v} * \frac{\partial c}{\partial x} \quad (2-29)$$

Rearranging this equation to a dimensionless form leads to equation 2-30 using 2-31 for dimensionless time Θ and 2-32 for dimensionless time length z .

$$\frac{\partial c}{\partial \Theta} = \left(\frac{D_{ax}}{\bar{v}L} \right) \frac{\partial^2 c}{\partial z^2} - \frac{\partial c}{\partial z} \quad (2-30)$$

$$\Theta = \frac{t}{\tau} = \frac{t\bar{v}}{L} \quad (2-31)$$

$$z = \frac{\bar{v}t + x}{L} \quad (2-32)$$

The dimensionless group $D_{ax}/\bar{v}L$ in equation 2-30 is defined as the dimensionless Bodenstein number (also shown in equation 2-33). The Bodenstein number is the ratio of the convective and the diffusive mass transfer. High Bo numbers indicate low dispersion and high convective mass transport. $Bo = 0$ indicates total axial backmixing which is assumed in ideal stirred tank reactors. A $Bo = \infty$ stands for ideal

plug flow. In literature various empirical correlations to predict the axial dispersion coefficient D_{ax} for different geometric extractor designs are available [16].

$$\frac{D_{ax}}{\bar{v}L} = \frac{1}{Bo} \quad (2-33)$$

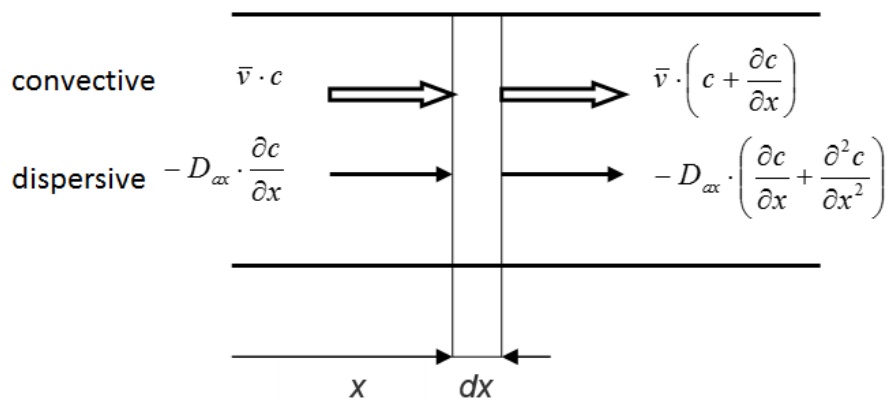


Fig. 2-14: Mass balance of finite volume element according to the dispersion model [16]

HTU-NTU Concept

To calculate the required height of extraction columns for a given separation efficiency the HTU-NTU concept is used. HTU indicates the height of one theoretical separation unit and NTU indicates the number of theoretical separation units. The concept is derived from inspection of finite volume cell. Calculation can be done according to equation 2-34, derived from the PFR design model. In this equation k indicates the overall mass transfer coefficient; A_Q is the cross sectional area of the column; \dot{F} is the volumetric flow and a_v is the specific mass transfer area of the dispersed phase. X defines the molar load of the valuable substance and X^* molar load at equilibrium state.

$$H = HTU * NTU = \frac{\dot{F}_v}{A_Q * k_R * a_v} \int_{X_\alpha}^{X_\omega} \frac{dX}{X - X^*} \quad (2-34)$$

Distinct axial backmixing decreases the separation efficiency of the column and thus need to be considered for column design. Since equation 2-34 does not consider axial backmixing the HTU*NTU model is extended with the HDU (height of dispersion unit) value as shown in equation 2-35. The HDU value can be calculated with the axial dispersion coefficient of the dispersed phase (index d) and continuous phase (index

c) . v stands for the superficial phase velocity of each phase. With the extended HTU*NTU model the column height can be calculated according to equation 2-37.

The axial dispersion coefficient of the continuous phase can be calculated using experimental data from residence time distribution (RTD). The RTD can be measured as mentioned above and is shown in figure 2-13. Empirical correlations are available to predict the axial dispersion coefficients. Kumar und Hartland [17] give an overview over empirical correlations for predictions of axial mixing coefficients in RDC columns. [3]

$$\overline{HTU} = HTU + HDU \quad (2-35)$$

$$HDU = \frac{D_{ax,c}}{v_c} + \frac{D_{ax,d}}{v_d} \quad (2-36)$$

$$H = \overline{HTU} * NTU \quad (2-37)$$

2.3.4 Design rules for the Taylor-Couette Disc Contactor

As mentioned in the previous section several empirical correlations, depending on the geometric design of the extraction column, are available in literature. This section will show design recommendation and empirical correlations for modeling and designing the TCDC extraction column.

Design recommendations for TCDC according to Aksamija [1]

Aksamija [1] optimized the TCDC design using CFD simulation and experimental validation. Final design recommendations are summarized in equation 2-38 to 2-40. Figure 2-15 illustrates a schematic drawing of the TCDC design.

$$d_R = (0,85 \dots 0,9) * D \quad (2-38)$$

$$d_{sh} \approx 0,5 * D \quad (2-39)$$

$$H_C = 2 * B_c \quad (2-40)$$

Correlation for drop size distribution and Sauter mean diameter

Grafschafter and Siebenhofer [18] defined a correlation to predict the Sauter mean diameter in TCDC columns. Several experiments in a TCDC column with 100 mm column diameter delivered the experimental data. Experimental DSD data was

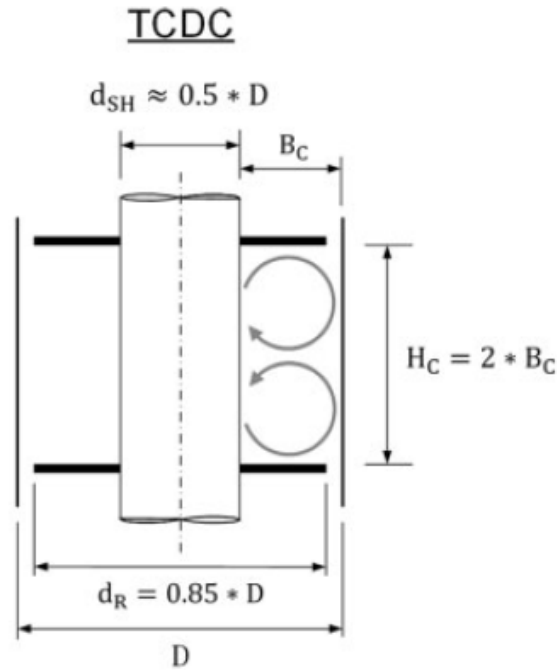


Fig. 2-15: Design recommendations TCDC [18]

recorded using an endoscope camera and automated pattern fitting algorithm by SOPAT GmbH. Prediction of the Sauter mean diameter can be performed by predicting the DSD using probability distribution functions. Graftschafter und Siebenhofer [18] compare experimental results from fitted lognormal, Gaussian (normal) and Weibull distribution function. Weibull (equation 2-41) distribution function provided the lowest average absolute error. DSD is affected to physical parameters according equation 2-42. Probability distribution functions are mostly based on two fitting parameters a, b . These two parameters represent the variance and the mean of the DSD.

Predictions for a and b are possible using the empirical equations 2-43 and 2-44. G comprises the constant dimensionless geometric data $D/d_R, d_{SH}/d_R, H_C/d_R$ and physical properties ρ_d/ρ_c and η_d/η_c . G remains constant for the specific material system. Parameters A, d and exponent c_1 can be fitted for specific probability distribution function

$$q_3(x) = \frac{a}{b} \left(\frac{x}{b}\right)^{a-1} \exp \left[- \left(\frac{x}{b}\right)^a \right] \quad (2-41)$$

$$DSD = f(d_R, D, d_{sh}, H_C; n; \rho_c, \rho_d, \nu_c, \nu_d, \sigma; g\Delta\rho) \quad (2-42)$$

$$a = A \left[G \left(\frac{d_R^2 g \Delta \rho}{\sigma} \right)^{c_1} \right] n + d \quad (2-43)$$

$$b = A \left[G \left(\frac{d_R^2 g \Delta \rho}{\sigma} \right)^{c_1} \right] n + d \quad (2-44)$$

The Sauter mean diameter d_{32} is calculated from the DSD according to equations 2-45 and 2-46. These equations define a_v as the volume based area of droplets with the sphericity ψ . Droplets are assumed to be rigid spheres. Due to this ψ is defined as 1.

$$a_v = 6\psi \int_{x_{min}}^{x_{max}} \frac{1}{x} q_3(x) dx \quad (2-45)$$

$$d_{32} = \frac{6}{a_v} \psi \quad (2-46)$$

The correlation for the direct prediction of d_{32} in a TCDC reactor is defined as 2-47 according to Grafschafter and Siebenhofer [18].

$$\frac{d_{32}}{dR} = AG \left(\frac{\sigma}{d_R^3 \rho_c n^2} \right)^{c_1} \left(\frac{g \Delta \rho}{d_R \rho_c n^2} \right)^{c_2} = AG \left(\frac{1}{We} \right)^{c_1} \left(\frac{1}{Fr} \frac{\Delta \rho}{\rho_c} \right)^{c_2} \quad (2-47)$$

Correlation for dispersed phase holdup

The dispersed holdup is affected by the geometry, rotational speed, physical properties and flow rates of both phases in the column (see equation 2-48). Dimension analysis results in equation 2-49.

$$\varphi = f(d_R, D, d_{sh}, H_C; \rho_c, \rho_d, \nu_c, \nu_d, \sigma; n; g \Delta \rho; \nu_c, \nu_d) \quad (2-48)$$

$$\varphi = G \left[C_1 + C_2 \left(\frac{(\nu_c + \nu_d)}{d_R n} \right)^3 \right] \left(\frac{1}{We} \right)^{0.673} \left(\frac{1}{Fr} \frac{\Delta \rho}{\rho_c} \right)^{-2.177} \quad (2-49)$$

As mentioned previously the constant parameter G comprises the dimensionless geometric data as shown in 2-46. Table 2-2 shows parameter C_1 and C_2 for low hydraulic load and high hydraulic load.

Tab. 2-2: Design parameter for hold-up correlation 2-49

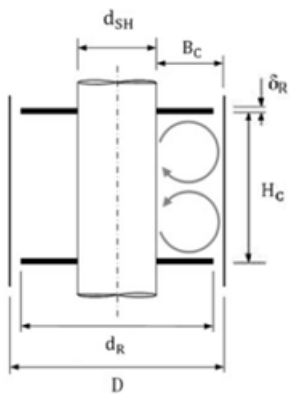
| | superficial-phase velocities [$m s^{-1}$] | C_1 | C_2 |
|---------------------|---|-------|----------------|
| low hydraulic load | $5.5 * 10^{-3} < (v_c + v_d) < 9.7 * 10^{-3}$ | 4.529 | $1.110 * 10^6$ |
| high hydraulic load | $(v_c + v_d) \geq 9.7 * 10^{-3}$ | 7.162 | $8.990 * 10^5$ |

3 Design and construction

This chapter is about the construction and implementation of a TCDC column with 300 mm column diameter, also called TCDC 300. To do this the internals of the the TCDC 300 column were designed according to the design rules mentioned in chapter 2. The geometric data of the column is summarized in table 5-2. The column was placed in a laboratory box and existing peripheral equipment such as tanks were integrated. The geometric data of the column evaluated according to Aksamija [1] is listed in table 3-1. All tubes and hose connections of the organic phase are made of polytetrafluorethylen (PTFE) to withstand chemical degradation. For the aqueous continuous phase PVC water tubes are used. All metal parts are made of stainless steel or brass. Friction bearings are used for the rotating shaft. The bearing material is specially designed to operate in liquid substances. The outer column cylinder is made of glass to ensure visual observation of the flow pattern. The column as well as the column periphery was designed in CAD (Pro/engineer). Figure 3-1 shows the TCDC 300 column mounted in the framework of the laboratory box. The space on the left side is used for the peripheral equipment. An engine is placed on the top of the column to drive the rotor of the TCDC.

Tab. 3-1: Rotor design TCDC 300 [1, 18]

| Recommendation for rotor design TCDC DN300 | | | |
|--|-------------------|-------|------|
| | Name | | Unit |
| Column diameter | D | 0,3 | m |
| Shaft diameter | d_{sh} | 0,15 | m |
| rotor disc diameter | d_R | 0,264 | m |
| thickness rotor discs | δ_R | 3 | mm |
| compartment height | H_c | 0,15 | m |
| active column height | H_{aktiv} | 1 | m |
| number of compartments | $N_{compartment}$ | 6 | - |



3.1 Rotor

This section explains the construction of the stirrer, which represents the core of the TCDC column.

The rotor consists of the following parts:

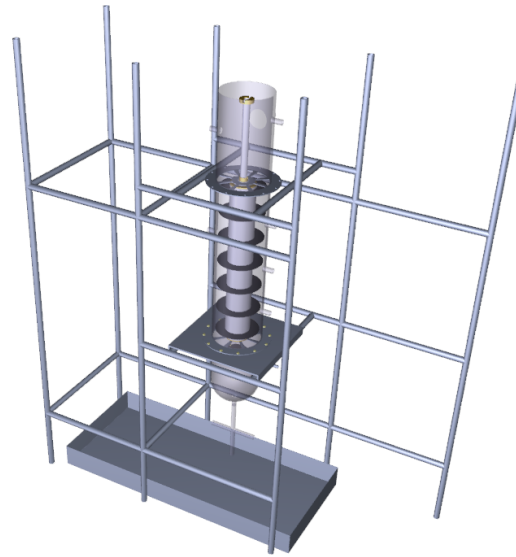


Fig. 3-1: Installed TCDC 300; the space on the left side is used for the peripheral equipment

- **Hollow shaft**
- **Discs**
- **Spacing Tubes**
- **Top cap and bottom cap**

All these parts except for the top cap are made of stainless steel (1.4301). To ensure disassembling of the rotor the top plate is made of brass (2.0401). The top and bottom cap are fitted with an o-ring seal to prevent liquid flowing into the hollow shaft. The weight of the rotor is reduced due to buoyancy force. This reduces the pressure to the friction bearings. Figure 3-2 shows the rotor of the TCDC 300 column. This rotor consists of the hollow shaft, discs, spacing tubes and the top and bottom cap. When assembling the rotor the spacing tubes were put over the hollow shaft alternating with the discs. Figure 3-3 shows the simple modular push-together system. The same shaft can be used for various designs. The rotor discs and spacing tubes can be changed to adjust the geometric design.

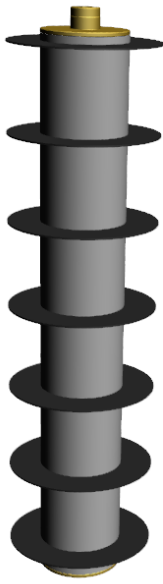


Fig. 3-2: TCDC 300 rotor

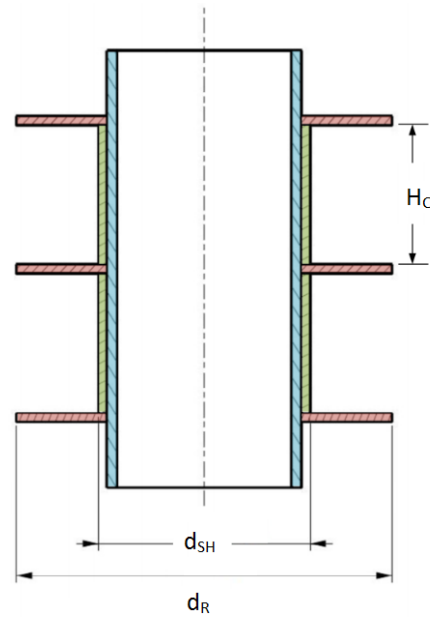


Fig. 3-3: Modular plug system of the rotor

3.1.1 Friction bearings

For the friction bearings the material iglidur®X is used. This material has a high resistance to chemicals and is specially designed for the use underwater. The bearing holder is designed for having minimal influence to the flow regime. More information about the used material can be found under [19]. Figure 3-4 shows the bearing plate with the installed friction bearing. The rotor/stirrer is mounted between two bearing plates in the column; one at the bottom and one at the top.

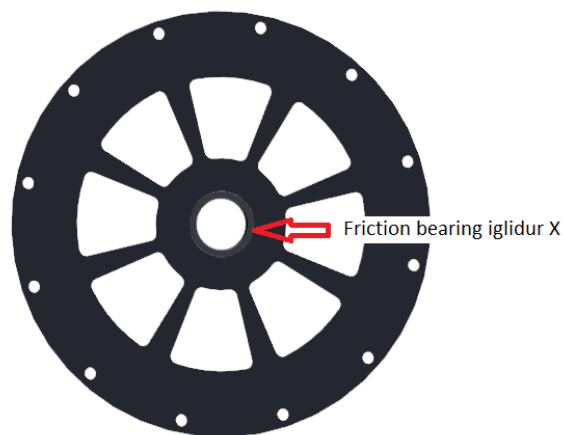


Fig. 3-4: Stainless steel bearing plate with the installed friction bearing made of iglidur®X

3.2 Column

The visible glass ensures visual observation of the flow pattern. Sampling along the column height is possible on 4 different positions. Figure 3-5 shows the three main glass parts of the column consist of the top part for phase separation (coalescence zone), the middle glass part where mixing takes place and the bottom glass part for the dispersion of the dispersed phase.

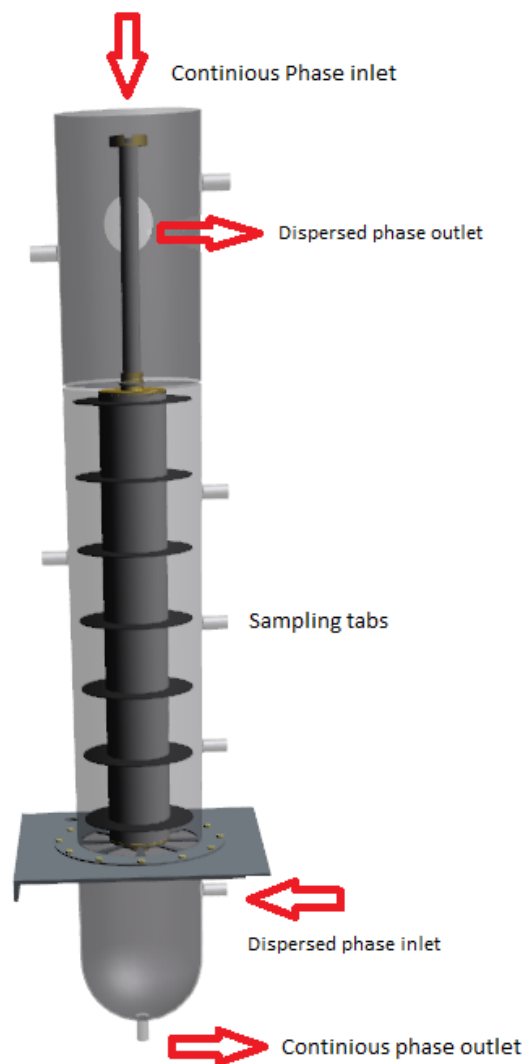


Fig. 3-5: TCDC 300 glass column with installed rotor

3.3 Disperser

At the bottom of the column a disperser with a diameter of 150 mm and 24 bores, each with a diameter of 4 mm, is placed, as shown in figure 3-6. The disperser guarantees

quick and homogeneous drop formation of the organic phase. Figure 3-6 shows the installed disperser in the lower glass part. The lower body of the disperser is made of PTFE. The top plate with its characteristic pattern is made of stainless steel. The droplet size of the organic phase at the inlet can be adjusted by changing the diameters of the bores in the top plate.

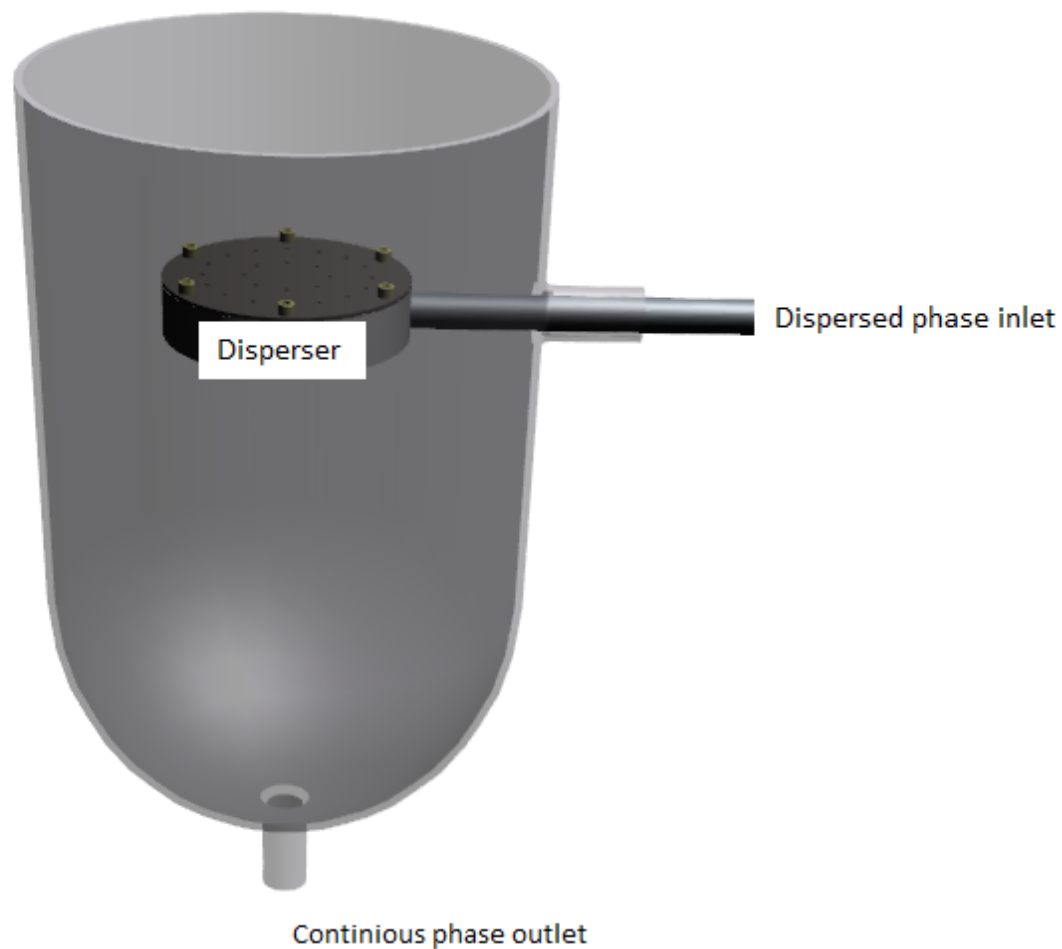


Fig. 3-6: TCDC 300 disperser in the bottom glass part

3.4 Peripheral devices

For hydraulic investigation the dispersed phase is circulated. For mass transfer experiments the dispersed phase can be pumped from the organic phase feed tank to the organic phase collection tank (raffinate tank). Operation modes can be changed by opening and closing valves according to the flow sheet 3-12. Figure 3-7 shows the peripheral equipment installed next to the column.

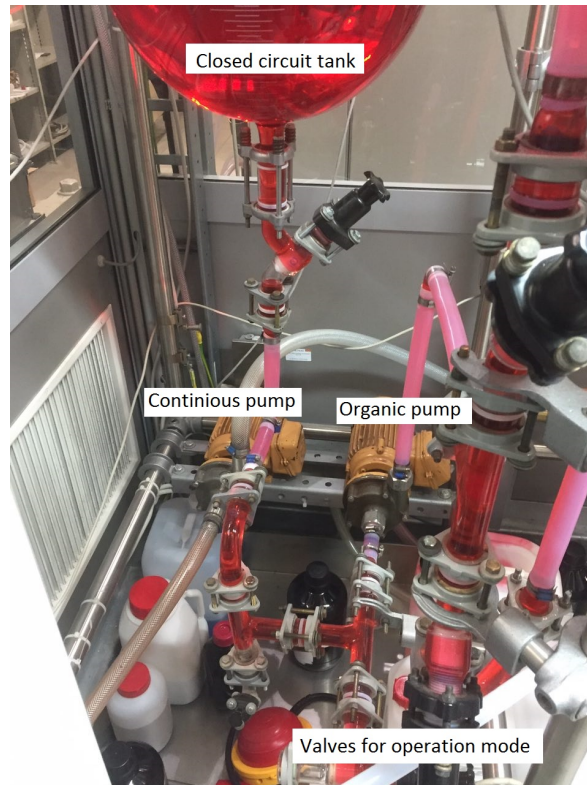


Fig. 3-7: Peripheral equipment: including pumps, valves for changing of operation mode and additional tank for closed circuit mode

3.4.1 Pumps

The necessary volumetric flow rate is about 630 l h^{-1} . Two centrifugal pumps are installed for pumping the liquid phases. For this column UP 130 centrifugal pumps from *Schmitt Kreiselpumpen* are used. The minimal diameter of all pipes is 25 mm. Figure 3-8 shows the characteristic curve (flow rate in relation to power or height) for this pump.

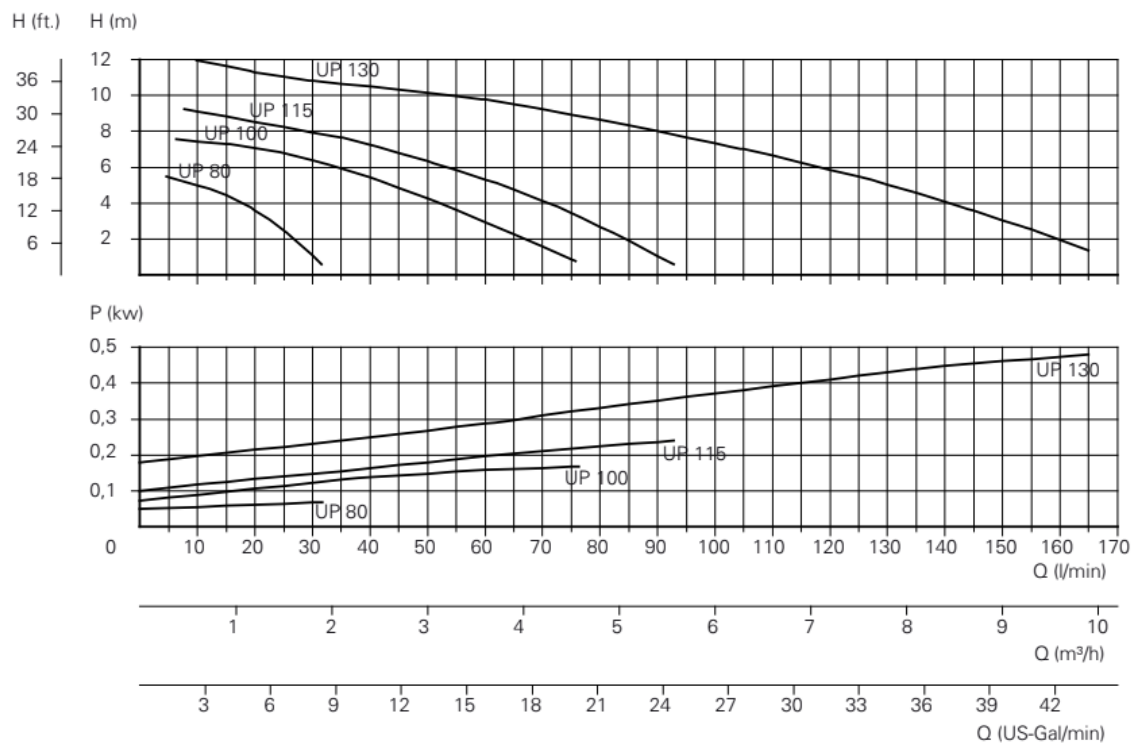


Fig. 3-8: Characteristic curve for centrifugal pump UP 130 [20]

3.4.2 Flow rate measurement

The volumetric flow rate is adjusted with a throttle valve. Coarse adjustment is done with the rotameter. For the fine adjustment up to 630 l h^{-1} two hypersonic flow rate sensors are used. Figure 3-9 shows the rotameter for each phase and the display unit of the hypersonic flow rate sensors. The caption of the flow rate sensors used and additional information can be found in the appendix 9.3

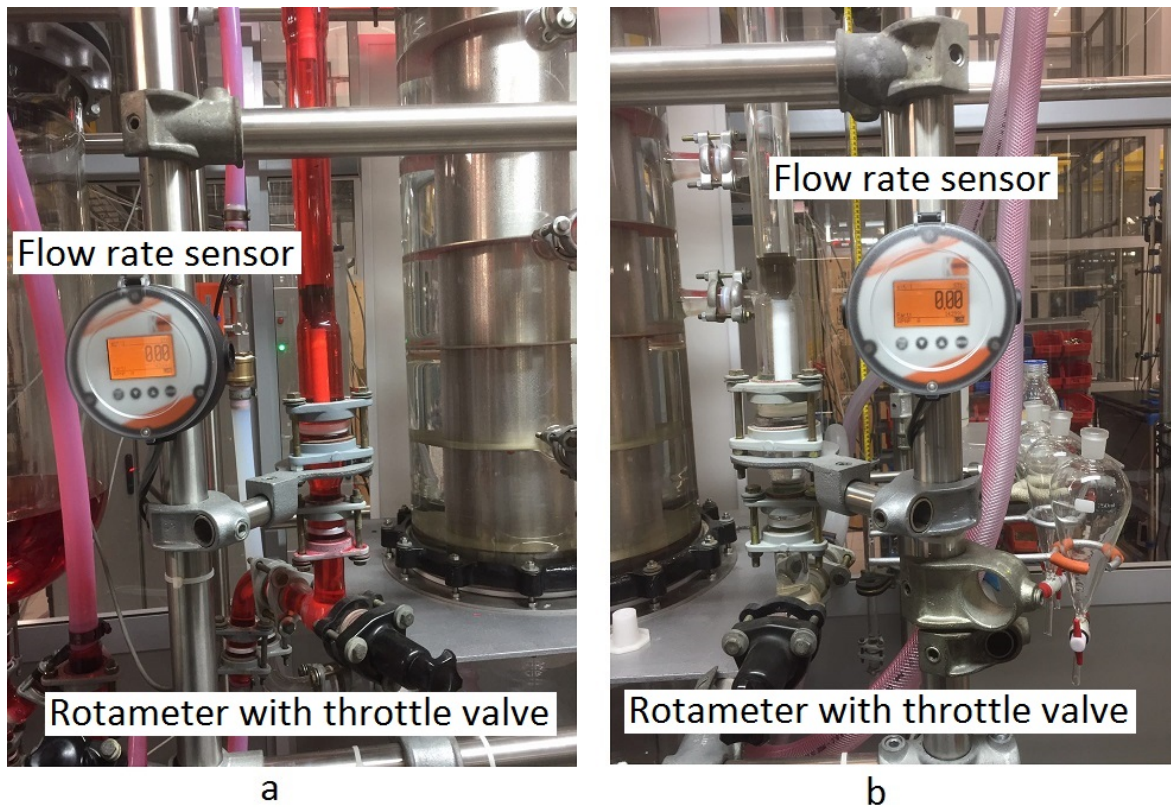


Fig. 3-9: Rotameter and digital display unit for hypersonic flow rate sensors; a: dispersed phase; b: continuous phase

3.4.3 Gear motor and rotational speed sensor

The rotor is turned using a gear motor (Figure: 3-10). This gear motor speeds up to a maximum rotational speed of about 300 rpm. The continuous variable gear provides the coarse adjustment. Fine adjustment of the rotational speed of the rotor can be done with the frequency converter. A hall sensor is used to measure the rotational speed. Two displays (Figure: 3-11) provide easy adjustment of rotational speed even of the gear on the top of the column and the frequency generator in the control box. The electronic circuit of the hall sensor is connected to an Arduino UNO. Additional information about the used circuit and code can be found in the appendix 9.5.

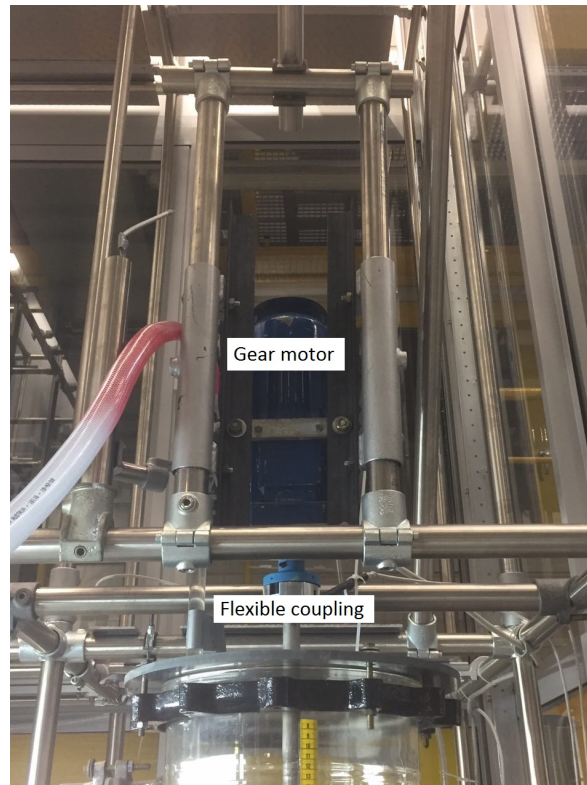


Fig. 3-10: Gear motor with installed coupling to connect the rotor to the motor



Fig. 3-11: left: Display next to the control box showing rpm and circumferential speed; right: Display next to the gear motor for coarse adjustment of rotational speed

3.5 Flowchart

The column can either be operated in circuit mode for hydraulic investigation or the dispersed phase can be collected after the extraction in an additional tank for mass transfer experiment. For hydraulic investigation mode the feed of the organic pump is

directly connected to the collection tank. For mass transfer experiments the receiver tank can be used as organic feed. Figure 3-12 shows the flow chart for both operation modes. The flow sheet can be also found in appendix 9.2

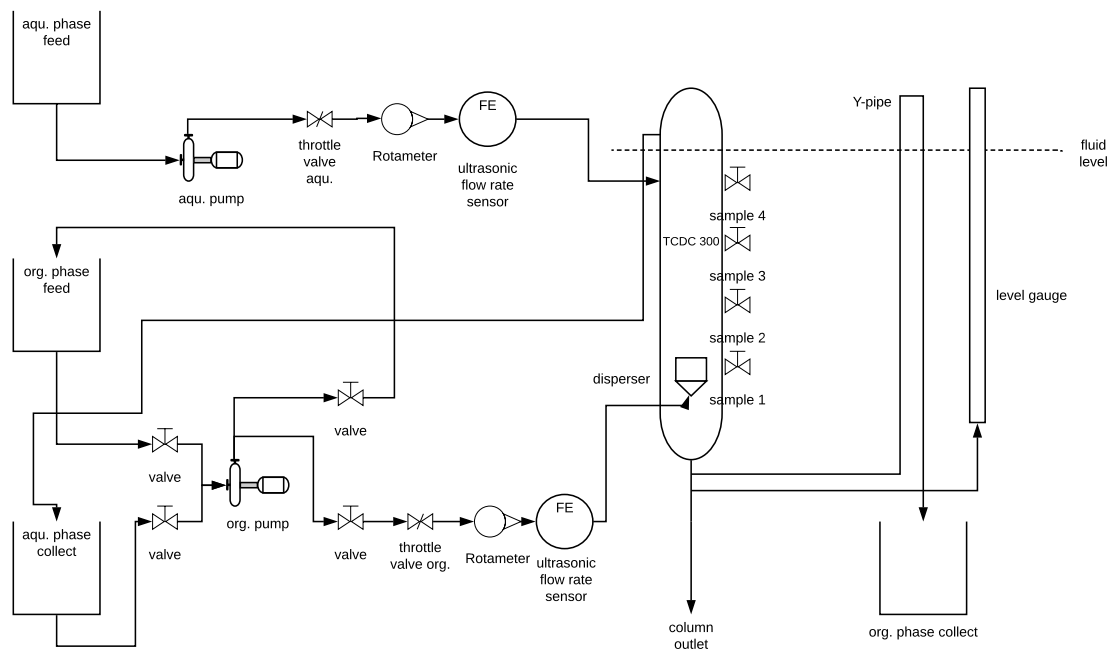


Fig. 3-12: Flow sheet of TCDC 300 plant

4 Initial startup

This chapter is about the initial operation of the TCDC column. Construction of the extraction column produces a lot of dirt in the entire column. Therefore the first step was to clean fat residues from manufacturing of the steel parts. The steel parts were cleaned with acetone. Subsequent all pipes are cleaned with deionized water and all connections are inspected to their leak tightness. Before the chemical test system is filled into the tanks and the column, initial operation is tested with deionized water.

4.1 Starting the column

After making sure that there are no leaks or other damage to the column, the organic phase was filled into the column. The aqueous phase was adjusted to a volumetric flow of about 250 l h^{-1} . After adding the organic phase with the equal volumetric flow, the phase boundary was adjusted with the Y-pipe. The gear motor was set to a speed of 150 rpm. After ensuring that all parts of the column work properly further tests were conducted. Figure 4-1 shows the flow pattern at the on-set speed of 150 rpm. At 150 rpm the vorticity of the toroidal vortex is stronger than the sedimentation force of the droplet. By increasing the rotational speed the banded two phase flow pattern gets more and more developed. In figure 4-2 the rotational speed is at 200 rpm and the hold up of the organic phase increases. The critical frequency of the rotor is at 260 rpm. At this frequency one can see obviously see vibration on the frame.



Fig. 4-1: TCDC 300 column at 150 rpm

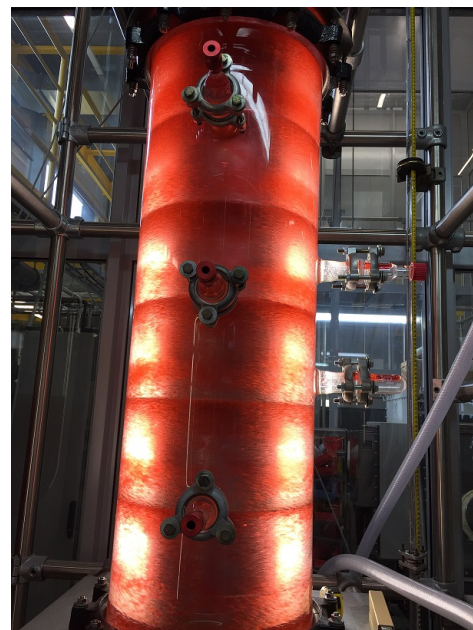


Fig. 4-2: TCDC 300 column at 200 rpm

4.2 Initial problems

At higher rotational speeds and high hydraulic loads the continuous phase at the outlet of the column gets into strong rotation and forms a maelstrom beneath the disperser, as shown in figure 4-3. The maelstrom carries the dispersed phase to the outlet of the continuous phase. This prevents the organic droplets from unhindered rising.

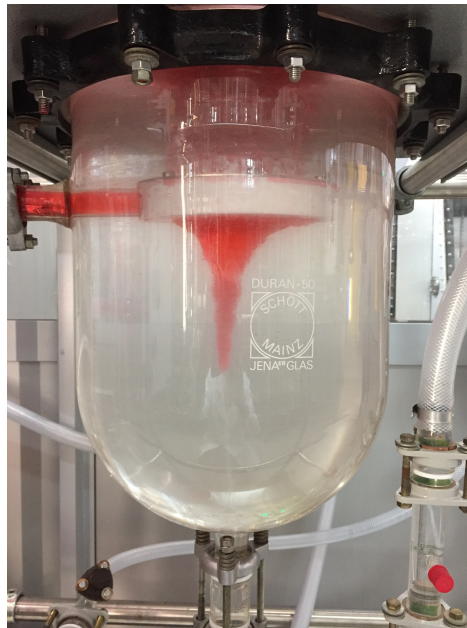


Fig. 4-3: Vortex formation at the aqueous phase outlet

To solve this problem a plain vortex breaker on the basis of a bathtub plug was constructed out of PTFE and placed in the outlet of the aqueous phase. Vortex breakers are very simple parts that prevent a vortex from entering the outlet of a vessel [21]. Figure 4-4 shows the column with installed vortex breaker at the outlet. Comparing this to figure 4-3 one can see that this simple construction works. The vortex is completely removed and the droplets can rise upwards.

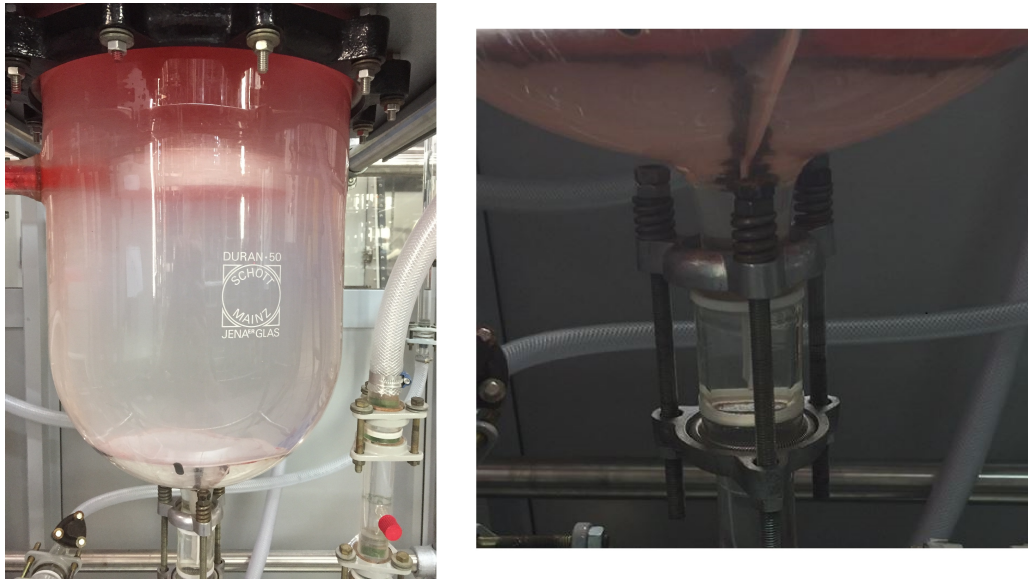


Fig. 4-4: left: Operating column with installed vortex breaker at the outlet of the aqueous phase; right: Detail of the vortex breaker installed at the outlet

4.3 Permissible operating limits

After the start up of the column the maximum hydraulic load of the column and rotational speed of the stirrer was determined. A maximum rotational speed of 300 rpm with a tip speed velocity of $4,15 \text{ m s}^{-1}$ is possible. For each phase a maximum volume flow rate of 630 l h^{-1} and thus a maximum hydraulic load of $B=25 \text{ m}^3 \text{ m}^{-2} \text{ s}^{-1}$ is possible. The limitation factor for the hydraulic load is the diameter of the continuous phase outlet at the bottom of the column. This 25 mm outlet is defined by the already existing glass parts for this column. Higher hydraulic loads are possible if the imitating outlet diameter and the diameter of the tubes are increased. At a rotational speeds of 260 rpm the column gets into resonant frequency. Due to very high vibrations this operation point should be avoided.

5 Experimental procedure

The hydrodynamic behavior of the TCDC 300 column was observed by measuring the dispersed phase holdup and droplet size distribution (DSD). All experiments were done at room temperature. The measured data was compared to existing data of the TCDC 100 column [1]. The correlations for prediction of holdup and Sauter mean diameter according to Grafschafter und Siebenhofer [18] were fitted and compared to the experimental data. For all experiments the test system Shellsol-T (SST) and deionized water was used. Deionized water was used as continuous phase and Shellsol-T was used as dispersed phase (technical data is given in the appendix 9.6). Shellsol-T was coloured red by adding a small amount of sudan red IV. This made the effect of flow pattern to the dispersed droplets more visible. Physical data of this binary system is given in table 5-1. The experiments were done in counter current operation. The dimensions of the TCDC 300 column are listed in table 5-2. Comparability between different column scales is provided by referring the measured data to the added power per volume (P/V). Rotational speeds for the scaled up TCDC 300 column that can be compared to the TCDC 100 column can be calculated according to equation 5-2. For equal input of power per volume the exponential factor m is set to $\frac{2}{3}$ according to table 5-3. The flow rates were adjusted to a total hydraulic load of $B = 15, 20, 25 [m^3 m^{-2} h^{-1}]$. Total hydraulic load B is calculated using equation 5-1. The dimensionless phase ratio of continuous to dispersed phase (w/o) varies from 0,5 up to 2. w (waterous) defines the amount of continuous phase and o (organic) defines the amount of the dispersed phase. [22]

Tab. 5-1: Physical properties of the test system

| | Kinematic viscosity $\nu [m^2 s^{-1}]$ | Density $\rho [kg m^{-3}]$ |
|------------------------|---|-------------------------------|
| ShellSol T (dispersed) | $1.85 * 10^{-6}$ | 756.8 |
| DI Water (continuous) | $1.102 * 10^{-6}$ | 998.1 |

$$B = \frac{\dot{V}}{A_{free}} \quad (5-1)$$

where:

B = total hydraulic load $[[m^3 m^{-2} h^{-1}]$

A_{free} = Free net cross-sectional area $A_{Column} - A_{Shaft} [m^2]$

Tab. 5-2: Geometric design TCDC 300

| | TCDC300 |
|----------------------------|---------|
| $H_{Active} [m]$ | 1 |
| $D [m]$ | 0.3 |
| $d_{SH} [m]$ | 0.15 |
| $d_R [m]$ | 0.264 |
| $H_C [m]$ | 0.15 |
| $\frac{H_{Active}}{D} [-]$ | 3.33 |
| $N_C [-]$ | 6 |

Tab. 5-3: Exponent m for different scope of application. [23] In this Thesis constant P/V ratio is used

| Value of m | Constant parameter | Application |
|---------------|--------------------|-------------------------------|
| 1 | constant tip speed | same maximum shear |
| $\frac{2}{3}$ | constant P/V | Same power per volume |
| 0,5 | constant Re | equal viscous/internal forces |
| 0 | constant speed | equal mixing time |

$$\dot{V} = V_d + V_c [m^3h^{-1}]$$

$$n_{TCDC300} = n_{TCDC100} \left(\frac{d_{R_{TCDC100}}}{d_{R_{TCDC300}}} \right)^m \quad (5-2)$$

where:

n = Rounds per minute [rpm]

d_R = Rotor diameter [m]

m = defined at table 5-3

The scaling up of mixing reactors is well documented in *Handbook of Industrial Mixing* [23]. In this thesis the following definitions are used to refer the measured data to to specific input of power per volume:

The power consumption of an impeller is defined in as follows:

$$P = Np * n^3 * d_R^5 * \rho_c \quad (5-3)$$

The empirical correlation of the power number N_p according to Kumar und Hartland [24] can be used for rotating extraction columns

$$N_p = \frac{109,4}{Re_{rot} + 0,74} * \left(\frac{1000 + 1,2 * Re_{rot}^{0,72}}{1000 + 3,2 * Re_{rot}^{0,72}} \right) \quad (5-4)$$

where the impeller Reynolds number Re_{rot} is defined as: [23]

$$Re_{rot} = \frac{n * d_R^2 * \rho_c}{\mu} \quad (5-5)$$

Power per volume P/V is calculated by

$$\frac{P}{V} \quad (5-6)$$

V defines the free volume of one compartment with the free sectional area $D - d_{SH}$ (A_{free}) and height H_c of the compartment

(5-7)

5.1 Dispersed phase holdup

This section explains the measurement of dispersed phase holdup and shows the results of holdup experiments and investigations. The dispersed phase holdup φ is defined as the ratio of dispersed phase volume V_d to the total volume in the column. The total volume includes the volume of the dispersed phase V_d as well as the continuous phase V_c . The dispersed phase holdup was calculated using equation 5-11 according to the hydrostatic equilibrium method. The heights used are shown in figure 5-1. The height of the continuous phase h_1 in the level gauge (figure 5-3), the height of the phase interface h_2 shown in figure 5-2 (mixed phase) and overall height h_3 were measured for holdup calculation. The mean density of the mixed phase is defined according to equation: 5-10. The combination of equation 5-9 and 5-10 leads to equation 5-11. Variation of the rotational speed changes the dispersed phase holdup. Increasing rotational speed increases the dispersed phase holdup.

Knowledge of the dispersed phase volume in the column combined with the droplet size enables the calculation of the specific mass transfer area in the column.

$$(h_3 - h_2) * \rho_d = (h_3 - h_2) * \rho_{mix} + h_2 * \rho_d \quad (5-9)$$

$$\rho_{mix} = \frac{(V_c * \rho_c + V_d * \rho_d)}{(V_c + V_d)} \quad (5-10)$$

$$\varphi_d = \frac{h_2 * \rho_d - (h_2 - h_1) * \rho_c}{(h_3 - h_2) * (\rho_c - \rho_d)} \quad (5-11)$$

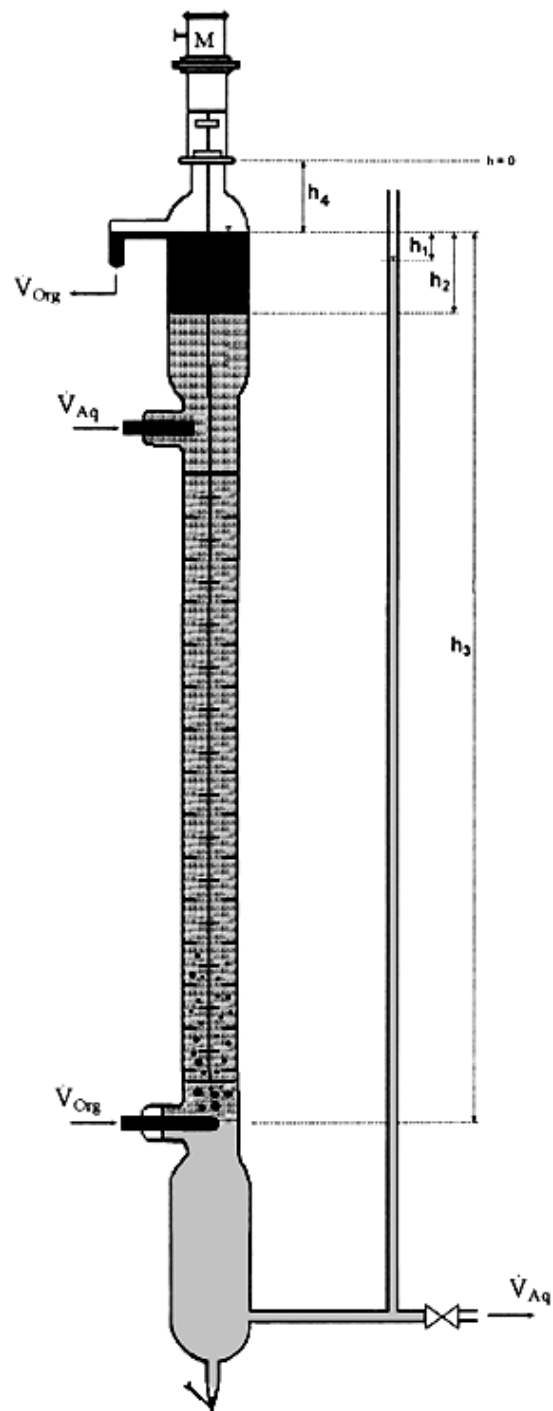


Fig. 5-1: Heights for measurement of dispersed phase holdup according to equation 5-11 [25]



Fig. 5-2: Height of phase interface h_2



Fig. 5-3: Height of the continuous phase h_1 in the level gauge

At maximum rotational speeds of 300 rpm and maximum total hydraulic load of $25[m^3m^{-2}h^{-1}]$ foaming occurs at the phase interface. The height of the foam area increases until it reaches the outlet of the dispersed phase. When the foam hits the outlet it collapses and starts growing again. To avoid foaming at the phase interface zone an increased diameter of the settler zone is needed. Due to that phenomena it was not possible to get accurate information about the hold up at very high rotational speeds as the phase interface was not clearly defined. The average height of the phase interface is used for these data points.

5.2 Drop size distribution

To get information about the specific mass transport area it is necessary to know the drop size distribution of the dispersed phase in the column. Combining this information with the holdup allows for calculation and prediction of the specific mass transfer area according to equation 2-45. An easy way to get information about the droplet size is image analysis. Optical measurement is based on taking pictures of single droplets. These pictures are analyzed by an automated pattern fitting algorithm. Droplets can not be photographed outside the column. Since droplets only exist in their actual condition and size, in the dynamic flow it is necessary to measure inline. Live data of the running process is needed to accuire the required information about the changing droplet diameter due to the changing rotational speed.

The company *SOPAT* provides special endoscope camera systems that can be used for inline particle or droplet size measurement. This system is very suitable for the drop size measurement in TCDC columns. The endoscope camera was installed at the sampling points that are distributed along the glass cylinder. Easy installation

is provided by using simple elastic sealing combined with GL18 fitting. Figure 5-4 shows the the endoscope camera in the running column. A reflector is mounted towards the lens of the camera. Different reflectors are available to optimize the contrast of the pictures for the specific application. Droplets that pass through the gap between the lens of the camera and the reflector are photographed. The light source is integrated in the endoscope camera and flashes for each picture. This enables the camera system to take pictures of single droplets. The frame rate can be adjusted to the rotational speed to ensure that droplets are only recognized once. The adjustable length of the camera system enables one to collect information about different areas of the vortex in the column. For these experiments the camera was placed close the surface of the glass cylinder. The endoscope measurement system only has a negligible influence to the flow pattern inside the column. Figure 5-5 shows how the camera system is installed at the column and the different measuring points. Sampling points that are not used are covered with a blind cap.

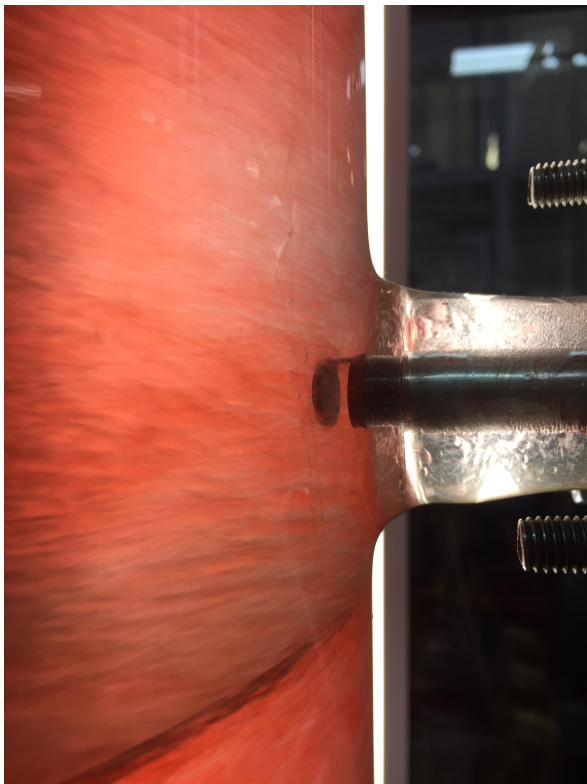


Fig. 5-4: Installed endoscope camera in detail

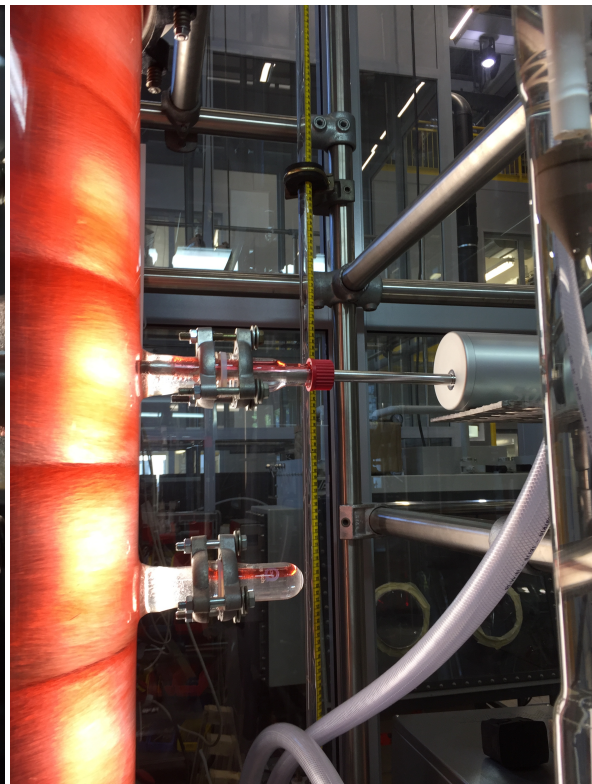


Fig. 5-5: Installation endoscope camera at the TCDC 300 column

With the *SOPAT* inline measurement system plenty of drop size data could be collected. The parameters for the automatic droplet identification algorithm are essential to the

quality of the results. The optimal parameters for these specific measurements were determined and provided by *SOPAT*.

For all experiments the endoscope camera "Pa3" by *SOPAT* is used. This camera can measure droplets with a size from 19,5 up to 2600 micrometer in an active field of view of 5,85 mm. More detailed information about the probe is given in the appendix at 9.4 [26].

The following reflector materials were tested before the parameters were optimized: No reflector, Rhodium and PTFE. PTFE delivered the best pictures with the highest contrast for this liquid phase system. Figure 5-6 shows the reflection of the droplets that occurs by using the rhodium reflector. These reflections (white spots in the picture) make it nearly impossible for the automated pattern fitting algorithm to identify the droplet and measure its correct diameter. Compared to rhodium PTFE delivers a better result. Figure 5-7 shows the picture done with the PTFE reflector. These pictures are much easier to measure by an automated algorithm. For all experiments the PTFE reflector is used with a set of optimized parameters for this specific task.

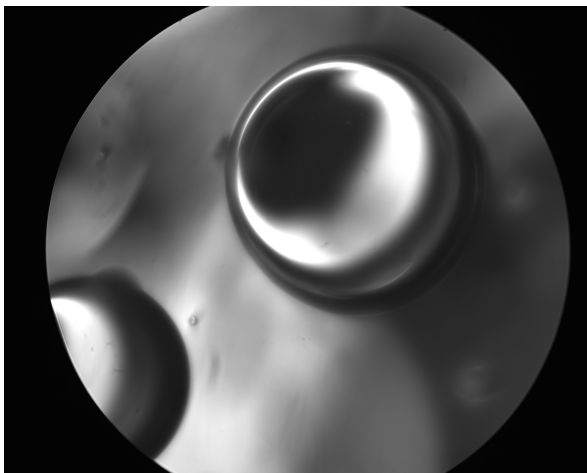


Fig. 5-6: Picture of the endoscope camera with the rhodium reflector

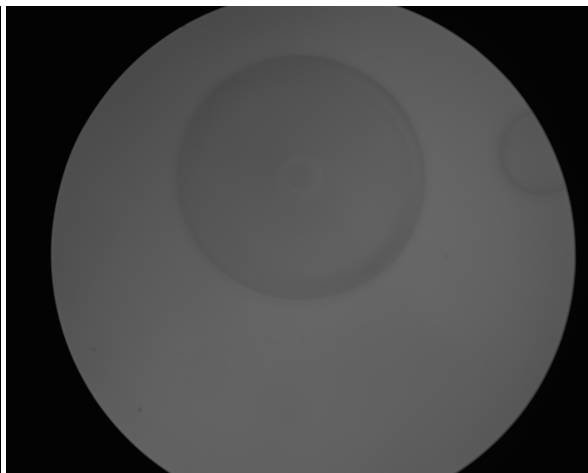


Fig. 5-7: Picture of the endoscope camera with the PTFE reflector

All measurements are performed in a stationary operation point. The column is stationary when the phase boundary layer remains constant. In most cases the column is stable after about 30 minutes. For all experiments five sets of pictures were recorded. Each set contains 200 high resolution pictures. All the pictures were analyzed by the *SOPAT* software. Figure 5-8 shows how the pattern fitting algorithm identifies the droplets. Droplets are automatically detected and measured. With this information the drop size distributions and the Sauter mean diameter can be determined. The output files can provide density histograms based on volume or

even number for instance. Sensitivity plots give information about the quality of the collected data. The Sauter mean diameter is used to calculate the available mass transfer area.

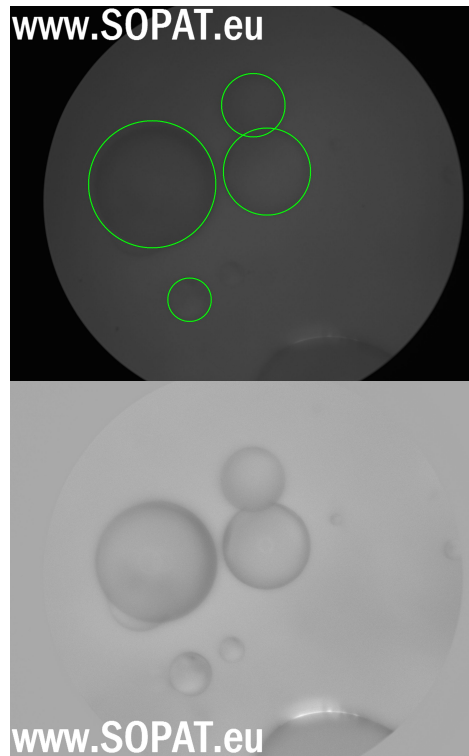


Fig. 5-8: Sample picture of the automated pattern fitting algorithm

6 Results and discussion

The measured holdup data and data of Sauter mean diameter is illustrated in diagrams. Significant data points are discussed and compared to data of the TCDC 100 column.

6.1 On-set and Flooding

With an increasing rotational speed of the rotor, the holdup of the dispersed phase increases, as shown in Figure 6-1. Increasing vorticity of the two toroidal vortexes leads to higher holdup values. The critical rotational speed is reached when the column gets blocked by the dispersed phase and starts flooding. A blocked operation state is indicated by a decreasing height of dispersed phase at the column outlet. At this operation state the dispersed phase accumulates down to the continuous phase outlet. This happens when the buoyancy of the droplets is much lower than the vorticity of the toroidal vortexes and thus the droplets cannot rise anymore. This point is called flooding point. Picture a to c in figure 6-1 shows the effect of increasing vorticity of the toroidal vortexes on the dispersed phase. In picture a and b the vorticity is lower than sedimentation force, thus the dispersed phase rise unhindered resulting in low holdup values. At the critical rotational speed of 194 rpm (picture c) the vorticity is strong enough to hold the dispersed phase inside the compartment with moderate holdup values for a reasonable time. This point is defined as the on-set of the column.

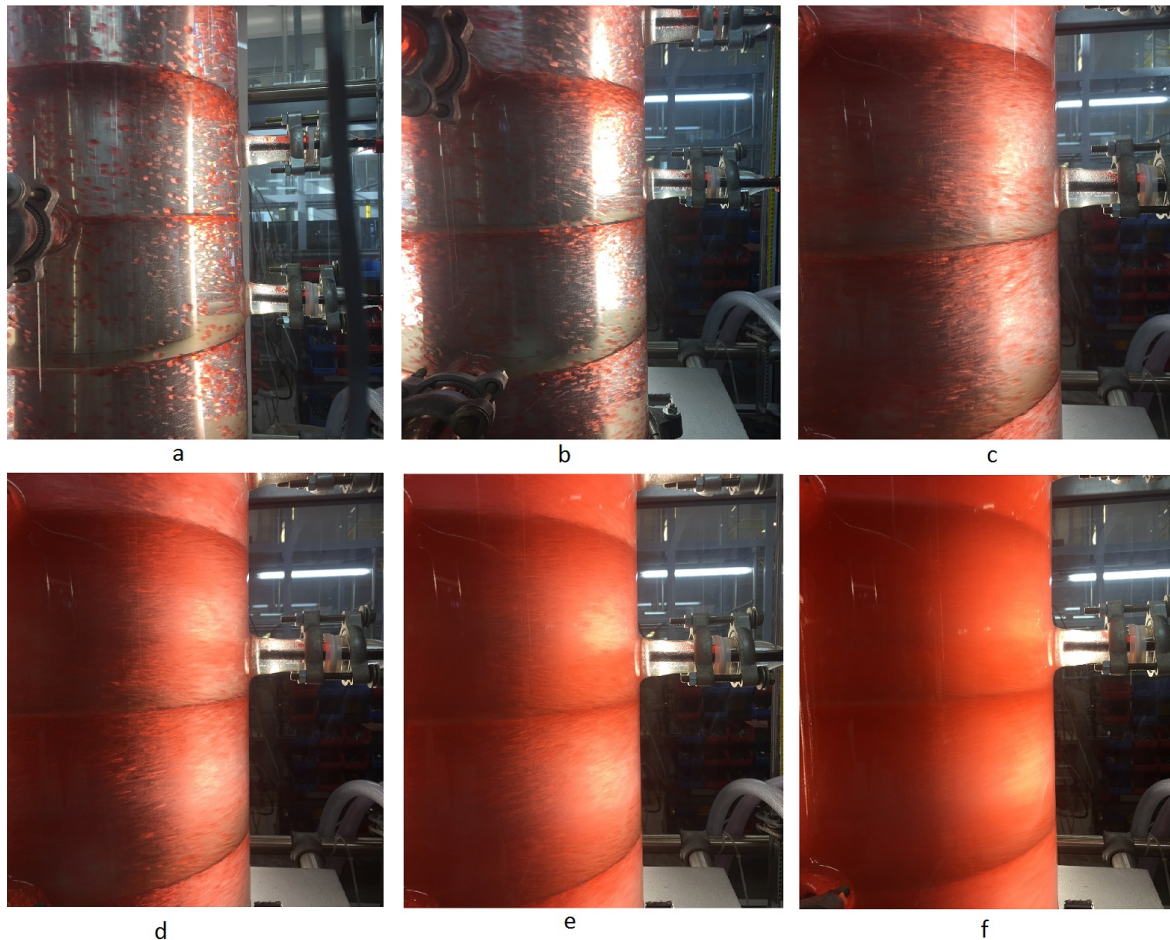


Fig. 6-1: Increasing holdup; volumetric flowrate for picture a to f: $V_{org} = 355 \text{ l h}^{-1}$ and $V_{aqu} = 705 \text{ l h}^{-1}$; rotation speed: a=95 rpm, b=145,5 rpm, c=194 rpm, d=218 rpm, e=242 rpm, f=280 rpm

6.2 Dispersed phase holdup

Table 6-1 summarizes the varying rotational speeds and volumetric flowrates for the holdup experiments. Figure 6-3 to 6-7 show the increasing holdup of the dispersed phase due to increasing rotational speed. There is a critical rotational speed at about 120 rpm where the holdup starts rising significantly. This point is called on-set point. The listed rotational speeds are defined according to equation 5-2. This provides comparable data that is based on equivalent input of power per volume. This data can be compared to existing data from the TCDC 100 column. Experimental holdup data for the TCDC 100 column is shown in 6-2. The total hydraulic load of $B = 20 \text{ [m}^3\text{m}^{-2}\text{h}^{-1}\text{]}$ is relatively low for the TCDC 300mm column. Previous holdup investigations in the TCDC 100 column indicated that for low hydraulic loads the influence of w/o ratio to the dispersed phase holdup can be neglected Graftschafter

et al. [22]. Investigation of low hydraulic load at $B = 20 [m^3 m^{-2} h^{-1}]$ in the TCDC 300 confirmed that w/o ratio is negligible. Figure 6-8 shows the influence of varying w/o ratio at constant low hydraulic load. The holdup increases progressively from the critical on-set rotational speed (120 rpm) up to 300 rpm. Rotational speeds above 300 rpm lead to the flooding of the column. Maximum holdup values in the TCDC column are reached at 17% and $B = 20 [m^3 m^{-2} h^{-1}]$.

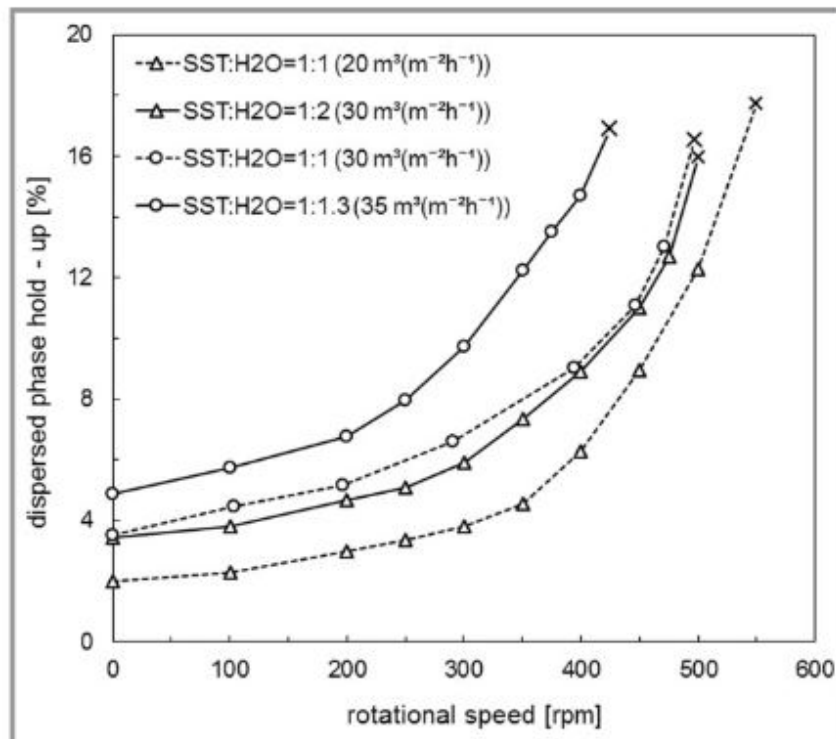


Fig. 6-2: Hold up Data for TCDC 100 column with different hydraulic load and rotational speed [18]

The following rotational speeds were observed at specific hydraulic loads and continuous (w) to dispersed (o) phase ratios (w/o):

Tab. 6-1: Operation points for hold up experiments

| n [rpm] | \dot{V}_{org} [$l h^{-1}$] | \dot{V}_{aqu} [$l h^{-1}$] | B [$m^3 m^{-2} h^{-1}$] | w/o |
|----------------------------------|--------------------------------|--------------------------------|-----------------------------|------|
| 0; 97; 145,4; 194; 218; 242; 291 | 706 | 353 | 20 | 0,5 |
| 0; 97; 145,4; 194; 218; 242; 291 | 634 | 425 | 20 | 0,67 |
| 0; 97; 145,4; 194; 218;242; 291 | 530 | 530 | 20 | 1 |
| 0; 97; 145,4; 194; 218;242; 291 | 424 | 636 | 20 | 1,5 |
| 0; 97; 145,4; 194; 218;242; 291 | 353 | 706 | 20 | 2 |

| | | | | |
|---------------------------|-----|-----|----|---|
| 121; 170; 218; 242,3; 280 | 397 | 397 | 15 | 1 |
| 121; 170; 218; 242,3; 280 | 530 | 530 | 20 | 1 |
| 121; 170; 218; 242,3; 280 | 662 | 662 | 25 | 1 |

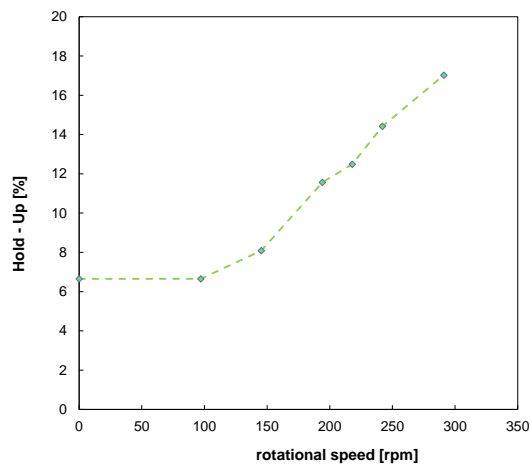


Fig. 6-3: Dispersed phase holdup for $B = 20 [m^3m^{-2}h^{-1}]$ and $w/o = 0,5$

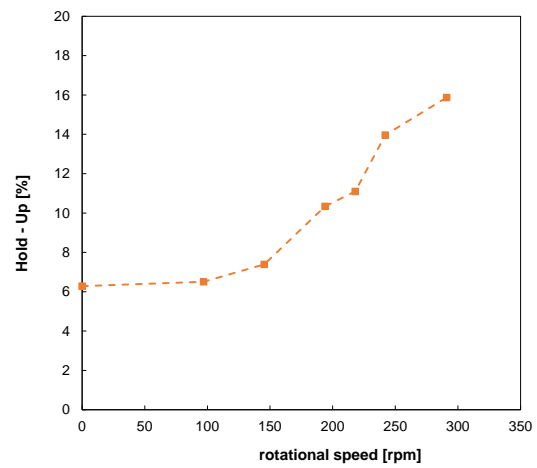


Fig. 6-4: Dispersed phase holdup for $B = 20 [m^3m^{-2}h^{-1}]$ and $w/o = 0,67$

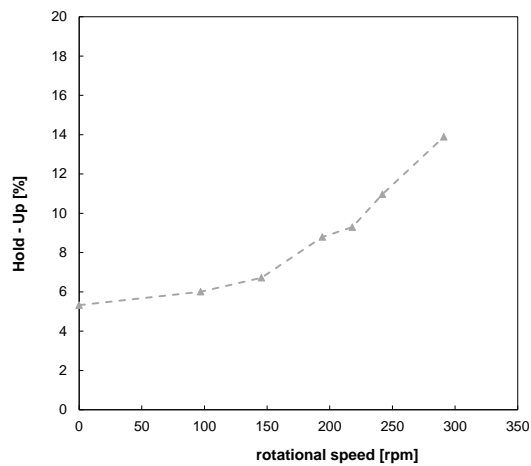


Fig. 6-5: Dispersed phase holdup for $B = 20 [m^3m^{-2}h^{-1}]$ and $w/o = 1$

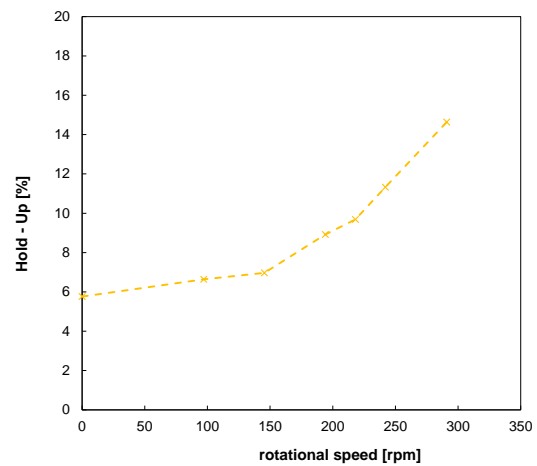


Fig. 6-6: Dispersed phase holdup for $B = 20 [m^3m^{-2}h^{-1}]$ and $w/o = 1,5$

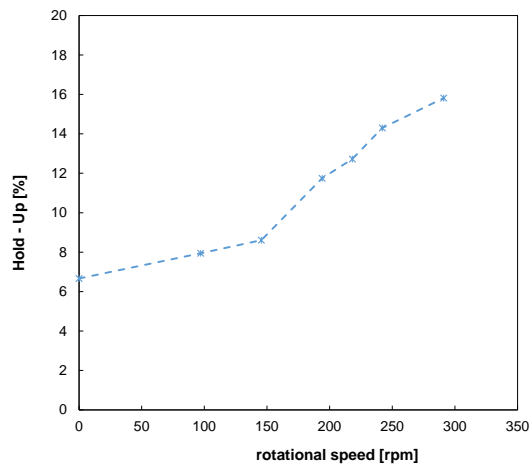


Fig. 6-7: Dispersed phase holdup for $B = 20 [m^3m^{-2}h^{-1}]$ and $w/o = 2$

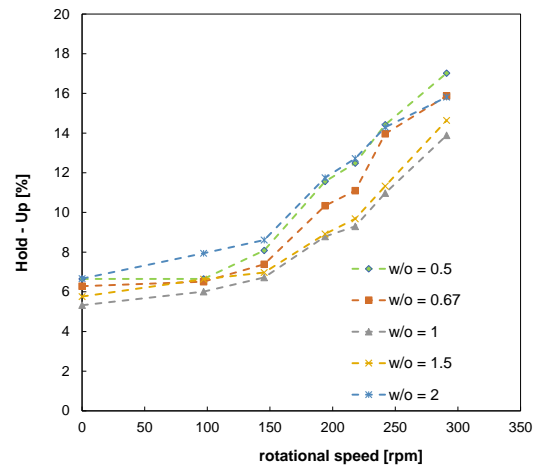


Fig. 6-8: Gathered dispersed phase holdup according to operation parameters listed in table 6-1 for constant hydraulic load of $B = 20 [m^3m^{-2}h^{-1}]$

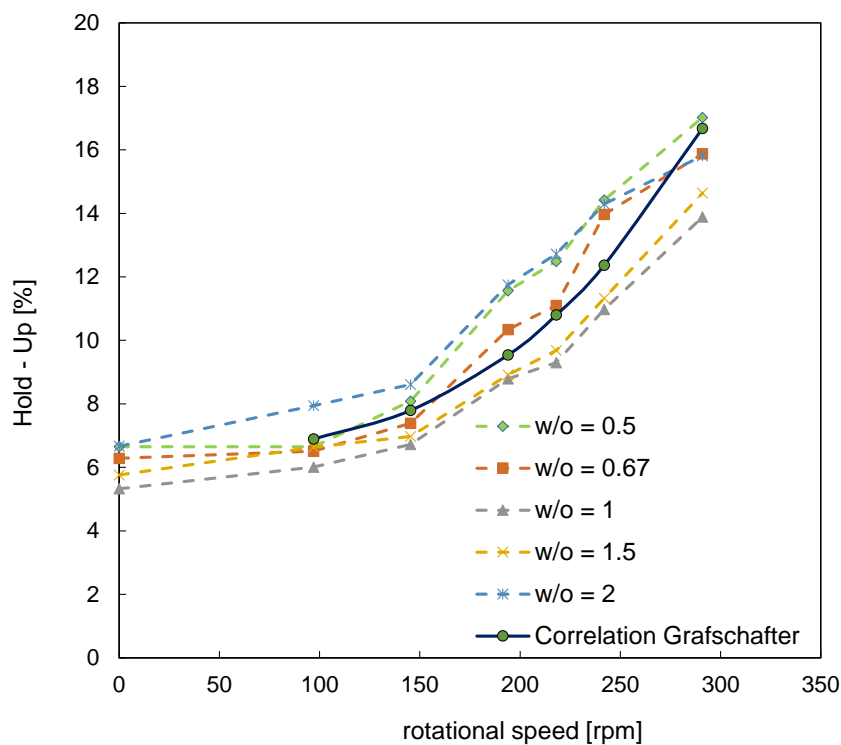


Fig. 6-9: Dispersed phase holdup at different w/o ratio and constant total hydraulic load of $B = 20 [m^3m^{-2}h^{-1}]$ including correlation according to Grafschafter and Siebenhofer [18]

Figure 6-9 shows the results of the TCDC 300 holdup experiments. Correlation 2-49 was applied to predict dispersed phase holdup at constant hydraulic load of

$B = 20 \text{ m}^3\text{m}^{-2}\text{h}^{-1}$. Parameters C1 and C2 are fitted for the experimental data (see table 5-3). G indicates the constant geometric column design. The correlation neglects the influence of varying w/o ratio at constant hydraulic loads. Predictions of dispersed phase hold up work for the scaled up TCDC 300 column. Parameters C1 and C2 have to be fitted separate for high hydraulic loads to get suitable results.

Tab. 6-2: Fitted parameter for holdup prediction according to equation 2-49 [18]

| Parameter | G [-] | C1 [-] | C2 [-] |
|-----------|-------|--------|------------|
| | 0,39 | 17,74 | 17680930,8 |

Comparison of TCDC 300 holdup results to already published holdup data of the TCDC 100 column [18] indicates that the TCDC 300 column shows higher dispersed phase holdup values at comparable rotational speeds (see figure 6-10). For comparability the holdup is plotted over input of power per volume (P/V ratio). The column scale up includes significantly higher dispersed phase holdup at same rotational speed. The conclusion for scaled up TCDC columns regarding to the disperse phase holdup is that empirical correlation according to Grafschafter und Siebenhofer [18] for dispersed phase holdup prediction deliver suitable results. In addition due to the increasing column diameter wall effects decrease and thus higher holdup values at same specific input of power per volume are possible. These aspects demonstrate that separation efficiency increases slightly with increasing column diameter.

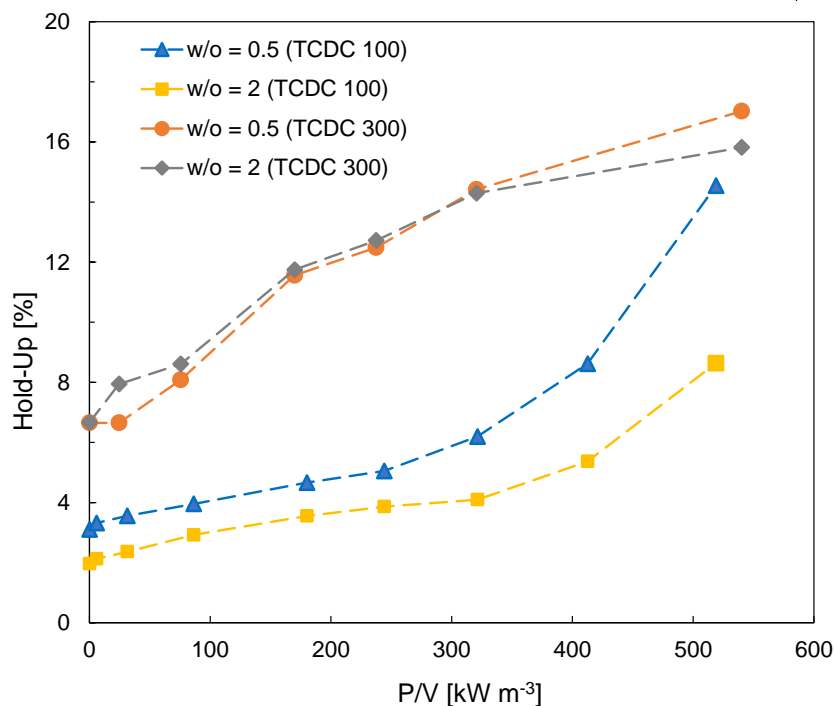


Fig. 6-10: Comparison of dispersed phase holdup in the TCDC 100 and TCDC 300 column at constant hydraulic load $B = 20 [m^3 m^{-2} h^{-1}]$ [22]

6.3 Sauter mean diameter and drop size distribution

Several operating points were determined before experiments were started. All the operation points are listed in table 6-3 and were observed at a stationary operation point. For low hydraulic loads and low rotational speed the flow pattern is not fully developed. This is the reason why the number of experiments varies with different hydraulic loads. The declaration of probe levels at the column is shown at figure 6-11. At level one DSD in the lower toroidal vortex is measured whereby at level three DSD in the upper toroidal vortex can be measured. Information about the DSD at the shear interface of the two toroidal vortexes can be gained at level 2 [22]. Phase ratio of continuous and dispersed phase remains constant during the experiments.

Tab. 6-3: Operation points for DSD determination at constant phase ratio:
w/o=1

| probe level | n [rpm] | V_{org}^* [$l\ h^{-1}$] | V_{aqu}^* [$l\ h^{-1}$] | B [$m^3m^{-2}h^{-1}$] |
|-------------|-----------|-----------------------------|-----------------------------|---------------------------|
| one | 242 | 265 | 265 | 10 |
| one | 280 | 265 | 265 | |
| one | 218 | 400 | 400 | |
| one | 242 | 400 | 400 | 15 |
| one | 280 | 400 | 400 | |
| one | 218 | 530 | 530 | |
| one | 242 | 530 | 530 | 20 |
| one | 280 | 530 | 530 | |
| two | 218 | 265 | 265 | |
| two | 242 | 265 | 265 | 10 |
| two | 280 | 265 | 265 | |
| two | 121 | 400 | 400 | |
| two | 170 | 400 | 400 | |
| two | 218 | 400 | 400 | 15 |
| two | 242 | 400 | 400 | |
| two | 280 | 400 | 400 | |
| two | 121 | 530 | 530 | |
| two | 218 | 530 | 530 | |
| two | 170 | 530 | 530 | 20 |
| two | 242 | 530 | 530 | |
| two | 288 | 530 | 530 | |
| two | 121 | 660 | 660 | |
| two | 170 | 660 | 660 | |
| two | 218 | 660 | 660 | 25 |
| two | 242 | 660 | 660 | |
| two | 280 | 660 | 660 | |
| three | 242 | 265 | 265 | 10 |
| three | 280 | 265 | 265 | |
| three | 218 | 400 | 400 | |
| three | 242 | 400 | 400 | 15 |
| three | 280 | 400 | 400 | |
| three | 218 | 530 | 530 | |
| three | 242 | 530 | 530 | 20 |
| three | 280 | 530 | 530 | |

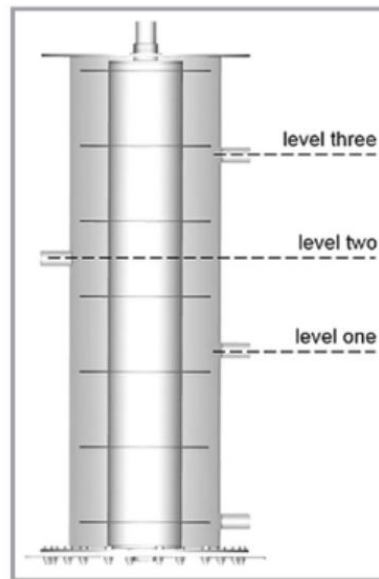


Fig. 6-11: Specification of probe levels [22]

Experimental data according to table 6-3 was recorded and evaluated by the *SOPAT* automated pattern fitting algorithm. Cumulative drop size distribution for probe level two at constant phase ratio $w/o=1$ and total hydraulic load of $B = m^3m^{-2}h^{-1}$ is illustrated in picture 6-13. With increasing rotational speed the droplet diameter shifts towards a smaller diameter. Influence of varying hydraulic load on drop size distribution is very low and negligible. Preceding experiments in the TCDC 100 column pointed that for low hydraulic loads there is no significant influence on drop size distribution [18]. Drop size distribution is primary defined by shear forces of the rotating discs. Power input per volume defines the characteristic drop size distribution for the selected rotational speed. The noticeable narrow drop drop size distribution in the TCDC 300 column can be explained due to lower wall effects for larger column diameters. Small scale columns need a significant amount of power to overcome wall friction which results in a wider drop size distribution. This effect is shown in the cumulative DSD of the TCDC 100 column (figure 6-13).

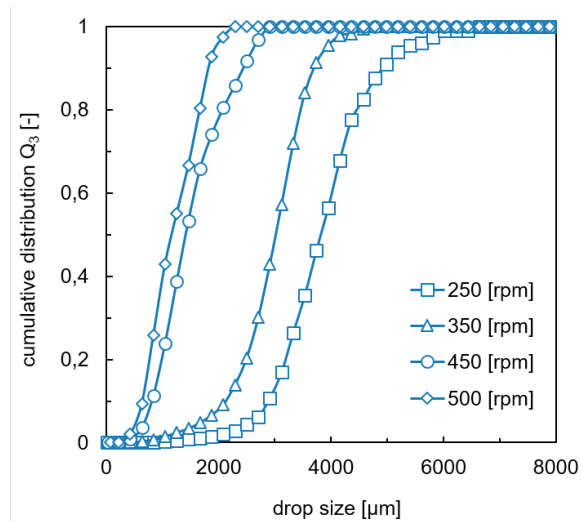


Fig. 6-12: Cumulative droplet size distribution for TCDC 100 column for varying rotational speed at constant $w/o=1$ and total hydraulic load of $B = 20 [m^3 m^{-2} h^{-1}] [1]$

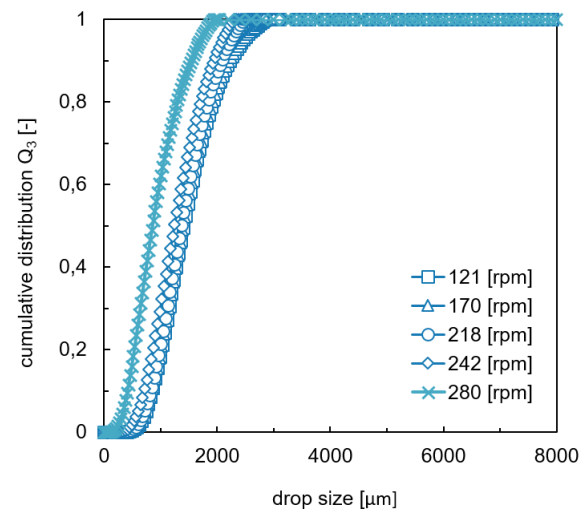


Fig. 6-13: Cumulative droplet size distribution for TCDC 300 column at probe level two for varying rotational speed at constant $w/o=1$ and total hydraulic load of $B = 20 [m^3 m^{-2} h^{-1}] [22]$

Sauter mean diameter d_{32} can be predicted using the empirical correlation 2-47. Parameters c_1 , c_2 and A are fitted for the TCDC 300 column. G remains constant and provide same dimensionless geometric data (table 6-4). For low rotational speeds droplet breakup is controlled by ratio of buoyancy to interfacial tension [22]. Due to that effect prediction parameters have to be fitted for two operation ranges. The onset operation range is up to $n_{crit} = 242 \text{ rpm}$ and fully developed operation range starts at $n \geq 242 \text{ rpm}$.

Tab. 6-4: d_{32} prediction parameters equation 2-46 fitted for the TCDC 300 column [22]

| Paramter | onset | fully developed operation |
|----------|-------|---------------------------|
| A | 3,45 | 2,56 |
| c1 | 0,67 | 0,59 |
| c2 | -0,57 | 0,39 |
| G | 0,39 | 0,39 |

Figure 6-14 compares the experimental Sauter mean d_{32} data to the predicted ones at different hydraulic loads and rotational speeds. Data of probe level two according to table 6-3 is used for comparison of experimental and predicted data. The predicted

Sauter mean diameters matches the experimental data. Prediction of Sauter mean diameter is possible and combined with predicted holdup of dispersed phase it is possible to predict the total mass transfer area. Investigations of varying hydraulic

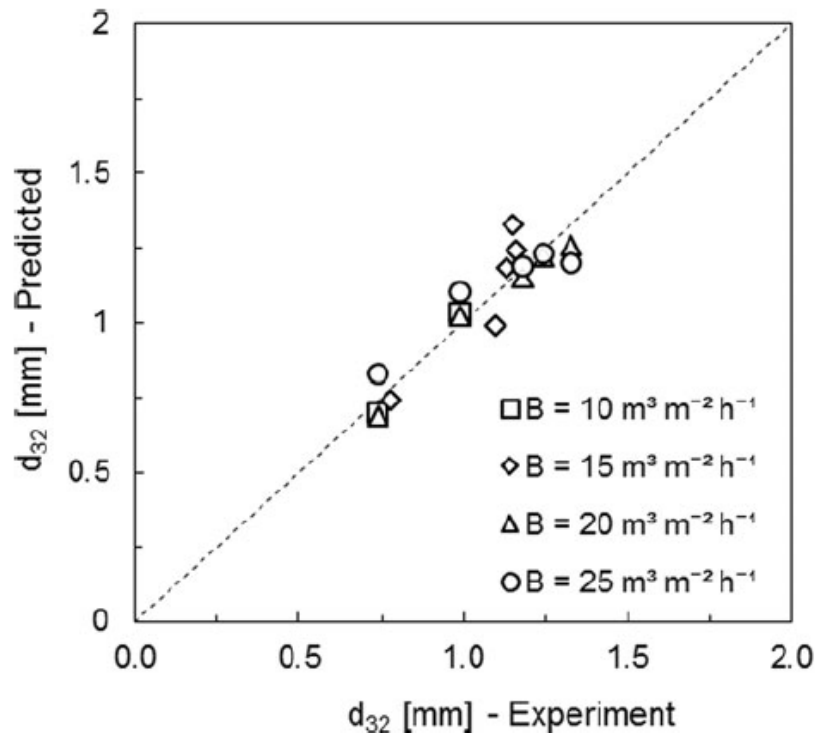


Fig. 6-14: Predicted and measured Sauter mean diameter for TCDC 300 using correlation 2-47 [22]

loads came to the same result as already observed in TCDC 100 column. The influence of hydraulic load on the Sauter mean diameter at constant rotational speeds is negligible. The effect of varying the hydraulic load is illustrated in figure 6-15. Exceeding critical rotational speed ($n_{krit} = 242 [rpm]$) leads to a significant reduction of droplet size. This reduction of droplet size occurs due to the force exerted by motion when the continuous phase overcomes the cohesive forces. The cohesive forces are defined by interfacial tension and viscosity of dispersed phase. Operation range below $n = 242 rpm$ is defined as onset operation range. Recommended operation range for the TCDC 300 column is from 242 rpm up to 300 rpm. Over-passing the maximum rotational speed leads to flooding of the column.

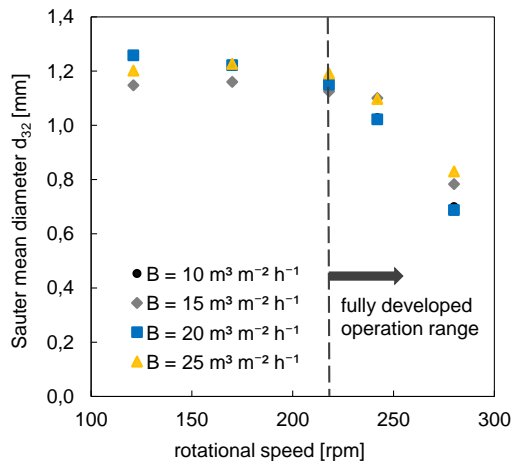


Fig. 6-15: Sauter mean diameter d_{32} probe level two for varying total hydraulic load B [22]

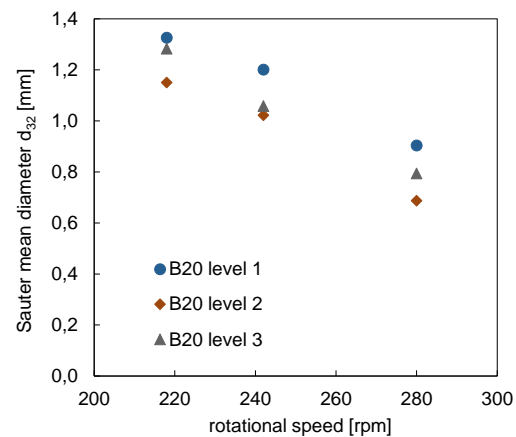


Fig. 6-16: Sauter mean diameter d_{32} for different endoscope camera level Graftschaffer et al. [22]

The influence of different probe levels on the DSD is shown in figure 6-11. Figure 6-16 describes the position of the endoscope in the compartment. The probe levels for the TCDC 300 columns were given due to the already existing glass component. Because of this it was not possible to investigate the Sauter mean diameter in one specific compartment as illustrated in figure 6-16. Comparing these three probe levels shows that Sauter mean diameter is significantly lower at level two. This is explained by higher shear and impact forces at the contact zone of the two toroidal vortices. The lower Sauter mean diameter of level three compared to level one is explained by a decreasing Sauter mean diameter along the column height. Level one is located in the third compartment of the column. From investigations of smaller column diameter we already know that about three compartments are necessary to have fully developed toroidal vortices and a stable DSD. It can be observed with the naked eye that the first compartment is not fully filled with dispersed phase and droplet diameter is bigger than in the compartments above. The first compartment acts as an inlet zone. Stabilized droplet size and flow pattern can be observed after the first three compartments. According to this Sauter mean diameter at level three is smaller than at level 1.

Comparing the data of the TCDC 300 column to the TCDC 100 column based on power per volume (figure 6-18 shows the influence of wall effects to the drop size distribution. At low rotational speeds a big influence of wall effects can be observed. At low power per volume the Sauter mean diameter in the TCDC 100 column is much higher than it can be observed in the TCDC 300 column. The influence of wall effects decreases with increasing column diameter. Preceding investigations of small scale

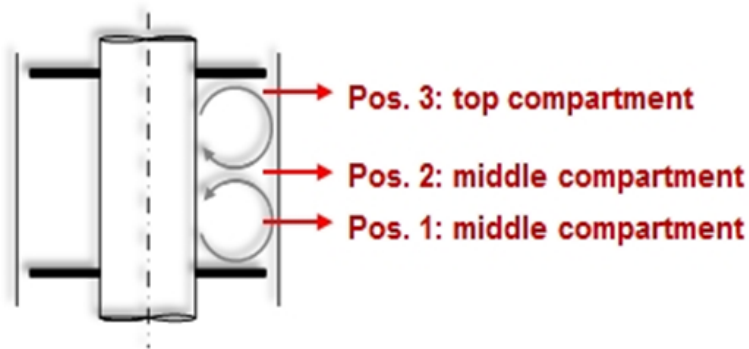


Fig. 6-17: Probe level in one compartment

columns done by Grafschafter [27] confirmed this observation. Applying the TCDC geometry to a column diameter of 30mm requires slightly convex bent rotor discs to ensure that the dispersed phase can rise up and is not hindered by wall effects and surface tension [27]. Increasing column diameter leads to less influence of wall effects. Additional positive effect of up scaled TCDC columns besides the increased hydraulic load is the increasing gap between wall and rotor disc. This gap allows to extract key components from liquid suspensions with larger solid particles.

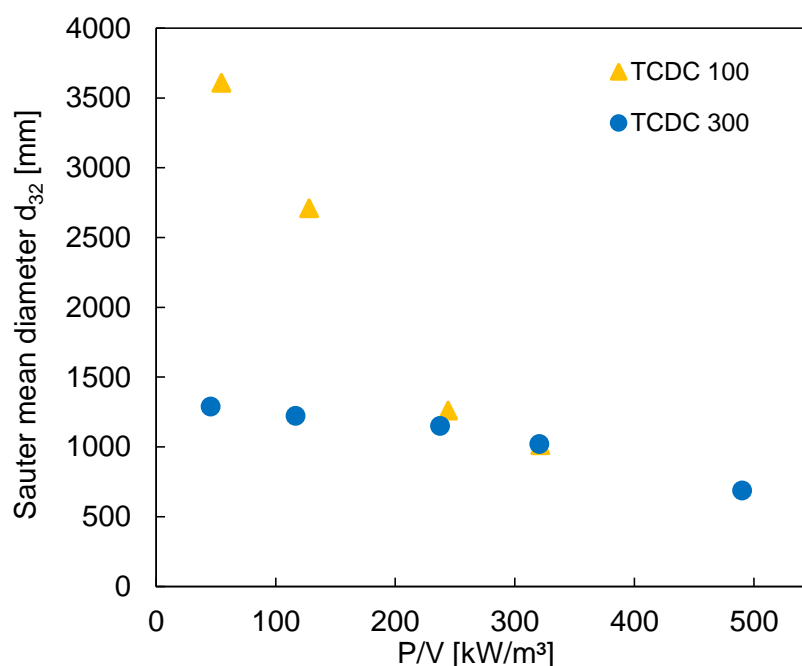


Fig. 6-18: Comparison of Sauter mean diameter d_{32} TCDC 300 and TCDC 100 plotted over power per volume (P/V)

7 Conclusion

The TCDC liquid-liquid extraction column design according to [1] was used to construct a TCDC column with a diameter of 300mm. Previous investigations of this simple geometric design that is based on the RDC design were done in a 100mm column. Data is available for columns with a diameter of 100mm [1]. The goal for this thesis was to scale up the TCDC column by factor of three referred to the diameter, construct this up scaled column, place it in operation and measure the dispersed phase hold up and droplet size distribution. The results were compared to existing data of the TCDC 100. Placing in operation an up scaled pilot plant generates teething troubles. Once proper functionality of this pilot plant was granted, experimental investigations started. The test system for hydraulic investigations was Shellsol-T as dispersed phase and deionised water as continuous phase. Dispersed phase hold up was measured by using principle of communicating vessels at static pressure equilibrium. Data was collected for rotational speed from 0 rpm to 300 rpm and total hydraulic load from $B = 15 [m^3 m^{-2} h^{-1}]$ up to $B = 25 [m^3 m^{-2} h^{-1}]$ at varying phase ratio. Higher total hydraulic loads are not possible with this experimental setup. The given cross section of the outlets limits the maximal volumetric flow rates. Experiments confirmed the expected increase in holdup due to increasing rotational speed. The on-set rotational speed defines the rotational speed when the dispersed phase holdup increases significantly for the first time. For the TCDC 300 column this speed is at 120 rpm. The influence of phase ratio can be neglected for low total hydraulic loads. Hydraulic load up to $B = 25 [m^3 / m^2 h]$ is relatively low for the TCDC 300 column. The maximal dispersed phase holdup in the experiments was at $\varphi = 17\%$. Prediction of the dispersed phase holdup works well using the correlation defined by Grafschafter und Siebenhofer [18]. Compared to experimental investigations on the TCDC 100 done by Grafschafter und Siebenhofer [18] the TCDC 300 column shows a significantly higher dispersed phase hold up for equal input of power per volume. The influence of higher hydraulic load should be investigated to confirm the significant influence of w/o ratio for high hydraulic load mentioned by Grafschafter und Siebenhofer [18]. An investigation of droplet size distribution was performed using an endoscope camera. This camera was placed in the column at different height. The endoscope camera system by *SOPAT GmbH* is designed for inline measurement of droplet- or particle-size distributions. The pictures that are taken by this endoscope camera system can be analyzed with an automated pattern fitting algorithm. Droplet size distribution shifts to smaller scale with increasing rotational speed. Compared to the DSD of the TCDC 100 column the TCDC 300 shows a significantly narrower DSD and lower Sauter mean diameter. This can be explained by the smaller wall effect in larger

columns. Small sized columns suffer from the problem that surface tension has a big impact on droplet size. These small sized columns tend to be blocked by the big dispersed phase droplets. In the TCDC 300 column droplet size shifts significantly smaller when the rotational speed exceeds $n_{crit} = 242 [rpm]$. At this speed the shear forces of the rotating discs overcome the cohesive forces. These cohesive forces stem from interfacial tension and viscosity of the dispersed phase. Optimal operation range for the TCDC 300 column is defined between 242 rpm and 300 rpm. Exceeding the maximal rotational speed leads to the flooding of the column. The prediction of the Sauter mean diameter according to Graesschafer und Siebenhofer [18] fits well. The influence of different probe levels can be explained by the increasing shear forces between the two toroidal vortexes in one compartment. In the middle of the compartment d_{32} is lower than on top or bottom of one compartment. Fully developed flow pattern is observed after the third compartment. Finally scale up of the TCDC design is possible. Up scaled TCDC columns are less sensitive to wall effects and surface tension. The next step is to measure the residence time distribution. Scale up of TCDC liquid-liquid extraction columns is possible. The increased diameter lowers side effects of cohesive forces. Finally, investigation of hydrodynamic behavior satisfies expectations.

8 References

8.1 References

- [1] Aksamija, E., 2014: *Der Taylor-Couette Disc Contactor (TCDC); ein vereinfachtes und optimiertes Design von Drehscheibenextraktoren*, TU Graz.
- [2] Grafschafter, A., Aksamija, E., Siebenhofer, M., 2016: *The Taylor-Couette Disc Contactor*, Chemical Engineering & Technology, 39(11), 2087–2095, URL: <https://onlinelibrary.wiley.com/doi/abs/10.1002/ceat.201600191>.
- [3] Sattler, K., 1995: *Thermal separation processes : principles and design*, VCH Publisher, New York, NY (USA), Germany.
- [4] Theodore, L., Ricci, F., Books24x7, I., 2010: *Mass Transfer Operations for the Practicing Engineer*, John Wiley and Sons, Incorporated, Hoboken.
- [5] Wankat, P.C., 2011: *Separation process engineering: includes mass transfer analysis*, Pearson Prentice Hall.
- [6] Mersmann, A., Kind, M., Stichlmair, J., 2005: *Thermische Verfahrenstechnik : Grundlagen und Methoden*, Springer, Berlin, Heidelberg, 2., wesentlich erweiterte und aktualisierte auflage. Auflage.
- [7] Kagan, S., Aerov, M., Lonik, V., Volkova, T., 1964: Journal of applied chemistry of the USSR, 37, 67–73.
- [8] Fischer, E., 1971: *Verfahrenstechnik*, 360–365.
- [9] Kumar, A., Hartland, S., 1986: *Prediction of drop size in rotating disc extractors*, The Canadian Journal of Chemical Engineering, 64(6), 915–924, URL: <https://onlinelibrary.wiley.com/doi/abs/10.1002/cjce.5450640605>.
- [10] Marr, R., Husung, G., Moser, F., 1978: *Verfahrenstechnik*, 12, 139–144.
- [11] Andereck, D., Liu, S., Swinney, H., 1986: *Flow Regimes in a Circular Couette System with Independent Rotating Cylinders*, Journal of Fluid Mechanics - J FLUID MECH, 164, 155–183.

- [12] Koerfer, S., 2002: *Der Einfluss von laminaren Strömungen und Sekundärströmungen im Taylor-Couette-System auf die Thrombozyten*, Technische Hochschule Aachen.
- [13] Chen, M., Xie, T., Xu, C., 2018: *Continuous counter-current centrifugal extraction column with high throughput using a spiral inner cylinder*, Chemical Engineering and Processing - Process Intensification, 125, 1 – 7, URL: <http://www.sciencedirect.com/science/article/pii/S0255270117309510>.
- [14] Stephan, P., Schaber, K., Stephan, K., Mayinger, F., 2017: *Thermodynamik: Grundlagen und technische Anwendungen - Band 2: Mehrstoffsysteme und chemische Reaktionen*, Springer Berlin Heidelberg, Berlin, Heidelberg, 16. Aufl. 2017. Auflage.
- [15] Kraume, M., 2011: *Transportvorgänge in der Verfahrenstechnik*, LinkSpringer Berlin Heidelberg, Berlin, Heidelberg.
- [16] Levenspiel, O., 1999: *Chemical reaction engineering*, Wiley, New York, NY [u.a.], 3.. Auflage.
- [17] Kumar, A., Hartland, S., 1992: *Prediction of axial mixing coefficients in rotating disc and asymmetric rotating disc extraction columns*, The Canadian Journal of Chemical Engineering, 70(1), 77–87, URL: <https://onlinelibrary.wiley.com/doi/abs/10.1002/cjce.5450700112>.
- [18] Grafschafter, A., Siebenhofer, M., 2017: *Design Rules for the Taylor-Couette Disc Contactor*, Chemie-Ingenieur-Technik, 4.
- [19] igus® GmbH, : *iglidur® X- Werkstoffdaten*, URL: <http://www.igus.at/info/plain-bearings-x-material-data>, (reviewed: 07.10.2018).
- [20] SCHMITT-Kreiselpumpen GmbH, : *Produktinformation Baureihe UP*, URL: http://www.schmitt-pumpen.de/uploads/media/Produktinfo_UP_01.pdf, (reviewed: 07.02.2017).
- [21] Sutton, I., 2017: *Chapter 4 - Piping*, I. Sutton, (Hrsg.) *Plant Design and Operations (Second Edition)*, 139 – 163, Gulf Professional Publishing, second edition. Auflage, URL: <http://www.sciencedirect.com/science/article/pii/B9780128128831000048>.

- [22] Graftschafter, A., Rudelstorfer, G., Siebenhofer, M., 2018: *Hydraulics and Operation Performance of TCDC-Extractors*, Chemie-Ingenieur-Technik, 90(6), 864–871.
- [23] Paul, E.L., Atiemo-Obeng, V.A., Kresta, S.M., 2004;2003;: *Handbook of Industrial Mixing: Science and Practice*, Wiley-Interscience, US.
- [24] Kumar, A., Hartland, S., 1996: *Unified Correlations for the Prediction of Drop Size in Liquid-Liquid Extraction Columns*, Industrial Engineering Chemistry Research, 35(8), 2682–2695, URL: <https://doi.org/10.1021/ie950674w>.
- [25] Gurker, T., 2010: *Experimentelle Charakterisierung einer gerührten Extraktionskolonne und Vergleich mittels Computational Fluid Dynamics*, , TU Graz.
- [26] SOPAT GmbH, : *Datenblatt Mesoskopsonde Pa*, URL: <http://sopat.de/de/sopat-mesoskopsonde-pa/>, (reviewed: 07.10.2018).
- [27] Graftschafter, A., 2014: *Hydrodynamik und Stoffaustausch in einem modifizierten Drehscheibenextraktor im Labormaßstab*, , TU Graz.

9 Appendix

9.1 Symbols used

| Symbol | Unit | Description |
|-------------|-----------------------|---|
| A | $[m^2]$ | mass-transfer area |
| A_Q | $[m^2]$ | cross-sectional column area |
| a | $[-]$ | parameter representing the variance |
| a_v | $[m^2m^{-3}]$ | specific mass transfer area |
| B | $[m^3m^{-2}h^{-1}]$ | total hydraulic load |
| B_C | $[m]$ | compartment width |
| b | $[-]$ | parameter representing the mean of the drop size distribution |
| c | $[mol\ m^{-3}]$ | concentration |
| c^* | $[mol\ m^{-3}]$ | equilibrium concentration |
| c_1, c_2 | $[-]$ | parameter |
| C_1, C_2 | $[-]$ | parameter |
| D | $[m]$ | column diameter |
| d_R | $[m]$ | rotor disc diameter |
| d_{32} | $[m]$ | Sauter mean diameter |
| d_R | $[m]$ | rotor diameter |
| d_{SH} | $[m]$ | shaft diameter |
| D | $[m^2s^{-1}]$ | diffusion coefficient |
| D_{ax} | $[m^2s^{-1}]$ | axial dispersion coefficient |
| f | $[Pa]$ | fugacity |
| \dot{F}_v | $[m^3m^{-1}]$ | volumetric flow |
| Fr | $[-]$ | Froude number, $d_R n^2 / g$ |
| g | $[m\ s^{-2}]$ | force of gravity, 9,81 |
| G | $[J]$ | Gibbs free energy |
| H_C | $[m]$ | compartment height |
| H_{DU} | $[m]$ | height of dispersion unit |
| H_{TU} | $[m]$ | height of one transfer unit |
| k | $[m\ s^{-1}]$ | overall mass transfer coefficient |
| K^* | $[-]$ | equilibrium constant |
| L | $[m]$ | length |
| n^* | $[mol\ m^{-2}s^{-1}]$ | specific molar flow |

| Symbol | Unit | Description |
|---------------|-----------------------|--|
| n | $[min^{-1}]$ | rotational speed |
| N^* | $[mol\ s^{-1}]$ | molar flow |
| N_C | $[-]$ | number of compartments |
| NTU | $[-]$ | number of transfer units |
| NTU | $[-]$ | number of transfer units |
| p | $[Pa]$ | pressure |
| Q_3 | $[-]$ | cumulative distribution |
| Q | $[J]$ | thermal energy |
| R | $[J\ mol^{-1}K^{-1}]$ | ideal gas constant |
| S | $[J]$ | entropy |
| T | $[K]$ | temperature |
| U | $[U]$ | inner energy |
| v | $[m\ s^{-1}]$ | superficial-phase velocity |
| V | $[m^3]$ | volume |
| V_R | $[m^3]$ | reactor volume |
| W | $[J]$ | work |
| We | $[-]$ | Weber number, $d_R^3\rho_c n^2/\sigma$ |
| X | $[-]$ | molar load |

Greek symbols

| | | |
|-----------|----------------|------------------------|
| β | $[ms^{-1}]$ | density |
| η | $[Pa\ s]$ | dynamic viscosity |
| ρ | $[kg\ m^{-3}]$ | density |
| σ | $[kg\ s^{-2}]$ | surface tension |
| φ | $[-]$ | dispersed-phase-holdup |
| ψ | $[-]$ | sphericity |

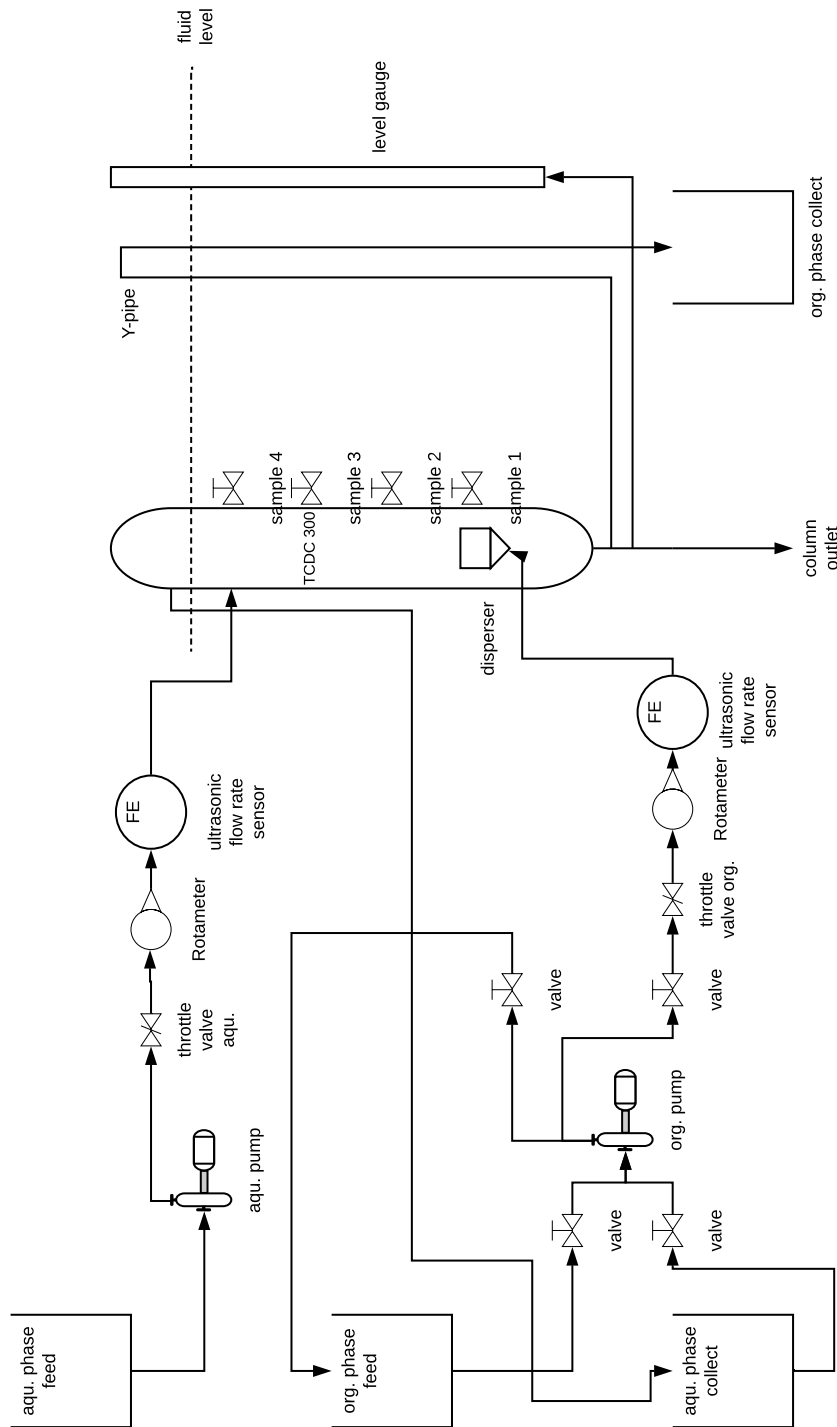
Subscripts

| | |
|-----|------------------|
| c | continuous phase |
| d | dispersed phase |

Abbreviations

| | |
|-------------|--|
| <i>CFD</i> | computational fluid dynamics |
| <i>CAD</i> | computer-aided design |
| <i>DSD</i> | drop size distribution |
| <i>PFR</i> | plug flow reactor |
| <i>PTFE</i> | polytetrafluorethylen |
| <i>PVC</i> | polyvinylchlorid |
| <i>rpm</i> | rounds per minute |
| <i>RDC</i> | Rotating Disc Contactor |
| <i>SST</i> | ShellSol-T |
| <i>TCR</i> | Taylor-Couette reaktor |
| <i>TCDC</i> | Taylor-Couette Disc Contactor |
| <i>w/o</i> | water (continious) to organic (dis- persed) phase ratio |

9.2 Flow sheet TCDC 300



9.3 Hypersonic flow sensor DUK-12-G4H-F300



Ultraschall Durchflussmesser / -wächter / -zähler -dosierer Typ DUK

Beschreibung

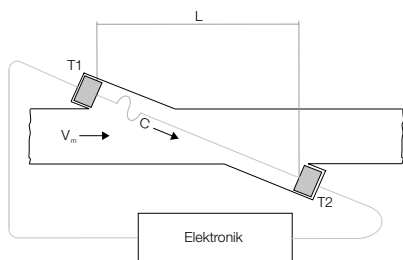
Die neuen KOBOLD Durchflussmesser des Typs DUK werden zum Messen, Überwachen, Zählen und Dosieren von niedrigviskosen Flüssigkeiten eingesetzt.

Die Geräte arbeiten nach dem Laufzeitdifferenzverfahren. Dies beruht darauf, dass Ultraschallwellen in einem Medium von der Fließgeschwindigkeit beeinflusst werden.

Zwei gegenüber, versetzt in der Rohrleitung montierte Sensoren arbeiten gleichzeitig als Sender und Empfänger von Ultraschallsignalen.

Ist kein Durchfluss vorhanden, so ist die Laufzeit der beiden Signale identisch. Bei fließendem Medium ist die Laufzeit gegen die Strömungsrichtung länger als die Laufzeit des Signales in Strömungsrichtung.

Die durch einen Mikroprozessor ermittelte Laufzeitdifferenz ist proportional der Fließgeschwindigkeit.



Die Geräte können mit einem Schalt-, Frequenz oder Analogausgang ausgerüstet werden. Außerdem steht eine Kompaktelektronik zur Auswahl, die eine Digitalanzeige, einen Schalt- und Analogausgang beinhaltet.

Abgerundet wird die Geräteserie durch eine optional erhältliche Dosier- und Zählelektronik. Die Zählelektronik zeigt in der ersten Zeile des Displays die momentanen Durchflussmenge und in der zweiten Zeile die Teil- oder Gesamtmenge an. Eine Dosierelektronik steuert einfache Abfüllaufgaben und misst ebenfalls Durchflussmenge, Gesamtmenge und Abfüllmenge. Zur Signalweiterverarbeitung können der Analogausgang und zwei Relaisausgänge verwendet werden.

Vorteile

- Hohe Messbereichsspanne von 1:250
- Geringer Druckverlust
- Hohe Wiederholgenauigkeit $\pm 0,1\%$ vom ME
- Unabhängig von Dichte und Temperatur

Einsatzbereiche

- Maschinenbau
- Automotive
- Robotertechnik
- Kühlung
- Heißwasser

Technische Daten

Sensor

| | |
|-----------------------|--|
| Messverfahren: | Ultraschall |
| Messbereich: | siehe Tabelle |
| Messstoffe: | Wasser mit max. 1% Feststoff |
| Viskosität: | max. 5 mm ² /s |
| Genauigkeit: | 0,7% vom MW + 0,7% vom ME |
| Wiederholgenauigkeit: | $\pm 0,1\%$ vom ME |
| Einbaulage: | beliebig, Durchfluss in Pfeilrichtung horizontaler Einbau: Elektronik nach oben oder unten) |
| Ein-/Auslaufstrecke: | 10 x DN |
| Messstofftemperatur: | -20 ... +90 °C -20 ... +120 °C (Hochtemperatur-Ausf.) |
| Umgebungstemperatur: | -20 ... +70 °C |
| Ansprechzeit t90: | ca. 0,5...1 s bei Strömungsänderungen > 10% ME (abhängig vom Elektroniktyp) |
| Druck: | 0 ... 16 bar |
| Druckverlust: | max. 150 mbar bei ME |
| Schutzart: | IP 65 |

Medienberührende Teile

| | |
|-------------------|--|
| Strömungsgehäuse: | Messing oder Edelstahl 1.4408 |
| Sensoren: | PEEK |
| Dichtung: | NBR, andere auf Anfrage Hochtemperatur-Ausführung FPM |

Messbereiche und Gewichte

| Typ | Messbereich [l/min] | Größe [G/NPT] | DUK-...S30x DUK-...F30x DUK-...Lxx3 | DUK-...C3xx | DUK-...Exxx DUK-...Gxxx | DUK mit ADI 24 V | DUK mit ADI 230/115/48 V |
|----------|---------------------|---------------|---|-------------|----------------------------|---------------------|-----------------------------|
| DUK-1xx4 | 0,08 - 20 | ½" | ca. 850 g | ca. 1050 g | ca. 1000 g | ca. 2150 g | ca. 2700 g |
| DUK-1xx5 | 0,16 - 40 | ¾" | ca. 1050 g | ca. 1250 g | ca. 1200 g | ca. 2350 g | ca. 2900 g |
| DUK-1xx6 | 0,25 - 63 | 1" | ca. 1450 g | ca. 1650 g | ca. 1600 g | ca. 2750 g | ca. 3300 g |
| DUK-1xx8 | 0,6 - 150 | 1½" | ca. 2350 g | ca. 2550 g | ca. 2500 g | ca. 3650 g | ca. 4200 g |
| DUK-1xx9 | 1 - 250 | 2" | ca. 3800 g | ca. 4000 g | ca. 3950 g | ca. 5100 g | ca. 5650 g |
| DUK-1xxB | 2,5 - 630 | 3" | ca. 7100 g | ca. 7300 g | ca. 7250 g | ca. 8400 g | ca. 8950 g |

Display for hypersonic flow sensor (ZOK-Z1-K-MF-3-0-0)



Dosier-, Zähl- und Überwachungselektronik Typ ZOK



Beschreibung

Die Elektronikseinheiten ZOK-Xx wurden speziell für die Berechnung, Anzeige und Übertragung von Summen und Durchflussraten von Durchflussmessern mit Puls- oder Frequenzausgängen entwickelt. Die Instrumente zeigen Flussrate, Tageszähler (rücksetzbar) und Gesamtzähler in den vom Bediener gewählten Maßeinheiten an. Eine übersichtliche mehrsprachige Menüführung leitet Sie durch die Programmierung der Geräte, wodurch der Blick in die Bedienungsanleitung größtenteils entfällt. Alle bedienerspezifischen Programmierungseinstellungen bleiben auch beim Batteriewechsel erhalten.

Die Elektronikoptionen ZOK-ZxK sind wetterbeständig und entsprechen Schutzart IP66/67 (Nema 4X), die Elektroniken sind in einem UV-beständigen, glasfaserverstärktem Nylongehäuse mit Edelstahlsschrauben und O-Ringdichtungen aus FPM untergebracht.

Die Option ZOK-ZxP befindet sich in einem Schalttafel-einbaugeschütz 96x96 mm in Schutzart IP44. Die Option ZOK-ZxF befindet sich in einem pulverbeschichteten Aluminium-Stranggussgehäuse mit Kunststoffdeckeln und entsprechender Schutzart IP66/67. Die Instrumente sind für raue Innen- bzw. Außenumgebungen geeignet und entsprechen EG-Richtlinie 2004/108/EG (Elektromagnetische Verträglichkeit).

Wesentliche Merkmale

- Batteriebetrieb- oder externe Versorgung, grafische LCD-Anzeige rückstellbarer und kumulativer Zähler, 5-stellige Hauptwertanzeige, konfigurierbar
- Robustes Feld- oder Panel montierbares Gehäuse
- Einfache Programmierung
- Universelle Impulseingänge
- Display Hintergrundbeleuchtung
- Statusausgang
- Skalierbarer Impulsausgang
- Optional: Wand- oder Rohrhalterung

Technische Daten

| | |
|---|---|
| Versorgungsspannung extern: | 5...28 V _{DC} (ohne Nutzung des Analogausganges) 8...28 V _{DC} (bei Nutzung des Analogausganges) 12...28 V _{DC} mit Relais max. Stromaufnahme: bei DC-Versorgung ca. 70 mA (mit voller Hintergrundbeleuchtung, ohne Ausgänge) |
| Ex-Ausführungen: | U _i = 28 V I _i = 100 mA P _i = 0,7 W |
| | <i>Siehe Tabelle auf Seite 7 für Einzelheiten</i> |
| Batterie (für Batteriebetrieb): | 3,6 V / 2200 mAh Lithium Größe AA |
| Batterielebensdauer im Batteriebetrieb: | abhängig vom eingestellten Sleep-Modus max. 17 Monate min. 3 Monate |
| Anzeige: | LCD, grafisch 128x64, Hintergrundbeleuchtung einstellbar (nur bei externer Versorgung) |
| Ziffernhöhe | |
| Hauptanzeigewert: | 12,5 mm |
| Anzeigauflösung | |
| Hauptanzeigewert: | 5-stellig, bezogen auf ME |
| Angezeigte Einheiten: | Liter, Milliliter, Gallons (US oder UK), Barrel, m ³ , benutzerdefinierte Einheiten |
| Eingangsskalierungsbereich: | 0,001 ... 99999,999 mit 3 gleitenden Dezimalstellen |
| Einbau: | Zählermontage, Wand-, Oberfläche-, Rohr- oder Schalttafel-einbau, Feldmontage |
| Messeingänge: | 2 x Pulseingang, Typ: NPN, PNP, NAMUR, Reed, Hall, Aktiv (per Software konfigurierbar) Eingangsfrequenz: 0,1 ... 1000 Hz, High-Low-Schwelle 1 V _{DC} , max. Eingangsamplitude 30 V _{DC} |
| Grundgenauigkeit der Durchsatzmessung: | <0,1 % des Messwertes (die Genauigkeit des angezeigten Wertes hängt von der eingestellten Skalierung und der Anzeigauflösung ab) |
| Sensorversorgung: | 8 V _{DC} , max. 30 mA (bei externer Versorgung > 10 V _{DC}) |
| Arithmetische Funktionen: | A + B, A - B mit skalierbarem Analogausgang |

9.4 Mesoscopic Probe SOPAT Pa3



| Produktkategorie | Pa |
|--|--------------------------|
| Messbereich [μm] | 19,5 – 2.600 |
| Sichtfeld [mm] | 5,85 |
| Tubuslänge [mm] | 100 – 2.000 |
| Tubusdurchmesser [mm] | 12 |
| Druckbereich [bar] | -0,1 - 320 |
| Temperaturbereich [$^{\circ}\text{C}$] | -50 – 450 |
| Umgebungstemperatur [$^{\circ}\text{C}$] | -10 – 40 |
| pH-Wert | 0 - 14 |
| Werkstoff Sondenfenster | Saphirglas |
| Werkstoff Sondentubus* | 1.4571 |
| Werkstoff Sondengehäuse | 1.4404 |
| Gewicht (ohne Kabel) [kg] | 4 |
| Fokussierung | Automatisch |
| Bildaufnahmerate [Hz] | 20 |
| Bildauflösung [MP] | 5 |
| Leistungsaufnahme [VA] | 140 |
| Zertifizierungen | CE, IP65, CIP/ SIP, ATEX |

* Sonderanfertigungen in folgenden Materialien möglich: 1.4401, 2.4602 (Hastelloy C22), Titan

9.5 Rotational speed sensor

9.5.1 Arduino UNO program

```

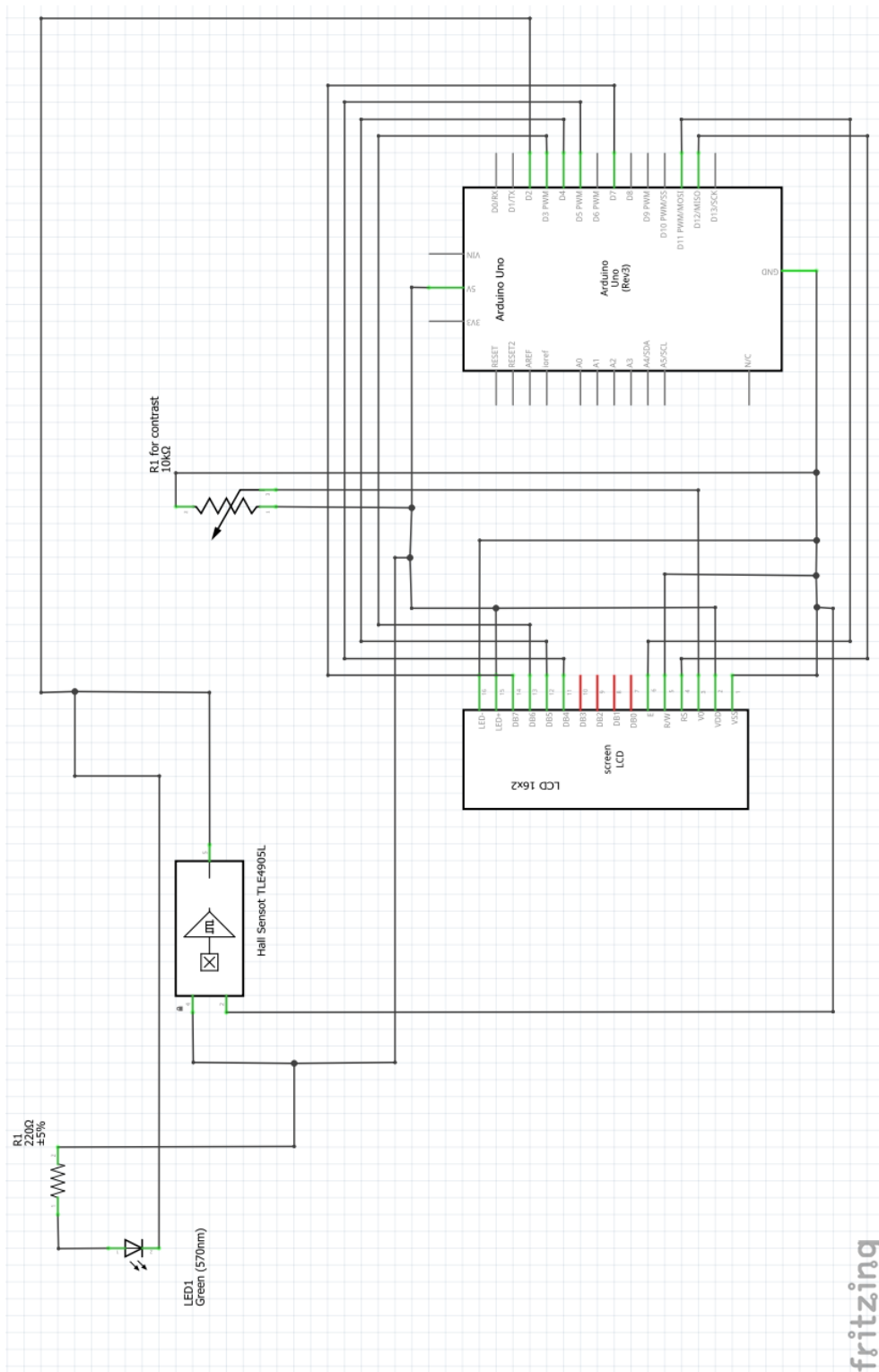
#include <LiquidCrystal.h>
LiquidCrystal lcd(12, 11, 5, 4, 3, 7);
volatile float time = 0;
volatile float time_last = 0;
volatile float rpm_array[5] = {0,0,0,0,0};
float sec=0;
void setup()
{
  Serial.begin(9600);
  //Interrupt 0 means digital pin 2
  attachInterrupt(0, impuls_interrupt, RISING);
  // set up the LCD's number of columns and
  rows:
  lcd.begin(16, 2);
  // Print a message to the LCD.
  lcd.print("Current RPM:");
}
void loop()
{
  float rpm = 0;
  while(1){
    //Slow Down The LCD Display Updates
    delay(400);
    //Clear The Bottom Row
    lcd.setCursor(0, 1);
    lcd.print("          ");

    //Update The Rpm Count
    lcd.setCursor(0, 0);
    lcd.print("n = ");
    lcd.print(rpm,1);
    lcd.print(" U/min      ");
    float v=0;
    float test=1.4567;
    lcd.setCursor(0,1);
    float pi=3.14;

    sec=rpm/60;
    v=sec*pi*0.264;
    lcd.print("vu = ");
    lcd.print(v,1);
    lcd.print(" m/s      ");
    Serial.print (rpm);
    ///lcd.setCursor(4, 1);
    ///lcd.print(time);
    //Update The RPM
    if(time > 0)
    {
      //Saving 5 data points to get the average
      rpm_array[0] = rpm_array[1];
      rpm_array[1] = rpm_array[2];
      rpm_array[2] = rpm_array[3];
      rpm_array[3] = rpm_array[4];
      rpm_array[4] = 60*(1000000/(time*1));
      //calculate average of 5 data points
      rpm = (rpm_array[0] + rpm_array[1] +
      rpm_array[2] + rpm_array[3] + rpm_array[4])
      / 5;
    }
  }
  //Capture interrupts
  void impuls_interrupt ()
  {
    time = (micros() - time_last);
    time_last = micros();
  }
}

```


9.5.2 Rotational speed sensor circuit




9.6 ShellSol-T technical data sheet

Shell Chemicals

Technical Datasheet

ShellSol T



| | |
|----------------------------|--|
| Product Code | Q7412 |
| Region | Americas |
| Product Category | Isoparaffins |
| CAS Registry Number | 64741-65-7 |
| EINECS Number | 265-067-2 |
| Description | ShellSol T is a synthetical isoparaffinic hydrocarbon solvent, characterised by a low odour. |

Typical Properties

| Property | Unit | Method | Value |
|--------------------------------------|----------------------|------------|--------------|
| Density @15°C | kg/L | ASTM D4052 | 0.761 |
| Coefficient of Cubic Expansion @20°C | 10 ⁻⁴ /°C | Calculated | 10 |
| Refractive Index @20°C | - | ASTM D1218 | 1.425 |
| Colour | Saybolt | ASTM D156 | +30 |
| Bromine Index | mg Br/100g | ASTM D1492 | 400 |
| Copper Corrosion (1hr @100°C) | - | ASTM D130 | 1 |
| Doctor Test | - | ASTM D4952 | Negative |
| Non Volatile Matter | mg/100ml | ASTM D1353 | 1 |
| Distillation, Initial Boiling Point | °C | ASTM D86 | 189 |
| Distillation, Dry Point | °C | ASTM D86 | 215 |
| Relative Evaporation Rate (nBuAc=1) | - | ASTM D3539 | 0.08 |
| Relative Evaporation Rate (Ether=1) | - | DIN 53170 | 110 |
| Antoine Constant A # | kPa, °C | - | 6.71506 |
| Antoine Constant B # | kPa, °C | - | 2009.16 |
| Antoine Constant C # | kPa, °C | - | 241.891 |
| Antoine Constants: Temperature range | °C | - | + 40 to +140 |
| Vapor Pressure @ 0°C | kPa | Calculated | 0.03 |

| | | | |
|---|---------------------------------------|--------------|-------|
| Vapor Pressure @ 20°C | kPa | Calculated | 0.11 |
| Saturated Vapor Concentration @ 20°C | g/m ³ | Calculated | 8 |
| Paraffins | % m/m | GC | >98 |
| Naphthenes | % m/m | GC | < 2 |
| Aromatics | mg/kg | SMS 2728 | 100 |
| Benzene | mg/kg | GC | < 3 |
| Sulfur | mg/kg | ISO 20846 | < 0.5 |
| Flash Point | °C | ASTM D93 | 61 |
| Lower Explosion Limit in Air | % v/v | | 0.6 |
| Upper Explosion Limit in Air | % v/v | | 6.0 |
| Auto Ignition Temperature | °C | ASTM E659 | 430 |
| Electrical Conductivity @ 20°C | pS/m | ASTM D4308 | < 1 |
| Dielectric Constant @ 20°C | - | - | 2.1 |
| Aniline Point | °C | ASTM D611 | 85 |
| Kauri-Butanol Value | - | ASTM D1133 | 26 |
| Pour Point | °C | ASTM D97 | < -50 |
| Viscosity @ 25°C | mm ² /s | ASTM D445 | 1.9 |
| Surface Tension @ 20°C | mN/m | Du Nouy ring | 24 |
| Thermal Conductivity @ 20°C | W/m/°C | | 0.13 |
| Hildebrand Solubility Parameter | (cal/cm ³) ^{1/2} | - | 7.4 |
| Hydrogen Bonding Index | - | - | 0 |
| Fractional Polarity | - | - | 0 |
| Heat of Vaporization at T _{boil} | kJ/kg | - | 250 |
| Heat of Combustion (Net) @t 25°C | kJ/kg | - | 45500 |
| Specific Heat @ 20°C | kJ/kg/°C | - | 2.0 |
| Molecular Weight | g/mol | Calculated | 171 |

(#) In the Antoine temperature range, the vapor pressure P (kPa) at temperature T (°C) can be calculated by means of the Antoine equation: $\log P = A - B/(T+C)$

List of Figures

| | | |
|------|---|----|
| 2-1 | Basic extraction process including solvent regeneration [5] | 3 |
| 2-2 | Overview of extraction operations and extractor designs. The red margin shows the focus of this thesis [3] | 5 |
| 2-3 | Figure (a) shows a "Kühni" column and figure (b) shows a Rotating Disc Contactor (RDC). Both designs use static internals to separate the column into compartments and to avoid backmixing. [3] | 7 |
| 2-4 | Toroidal vortex formation in a RDC Column [1] | 9 |
| 2-5 | left: plane Couette flow; right: cylindrical Couette flow [12] | 10 |
| 2-6 | Taylor-Couette flow in a TCR [13] | 10 |
| 2-7 | left: flow pattern in a RDC column; right: flow pattern in a TCDC column [1] | 11 |
| 2-8 | Molar free mixing enthalpy gives information about stability of binary mixtures: curve (a), stable mixture; curve (b), turning points get closer and define the critical separation point; curve (c), unstable system between W1 and W1 the miscibility gap is located between C1 and C2 [14] | 14 |
| 2-9 | Triangular diagram with two phase area. Below the binodal curve (\overline{CPD}) the mixture separates into two stable phases. Above the binodal curve the ternary mixture exists as one homogeneous phase. (\overline{CD}) is called tie line and defines the distribution of key component A in the two phases. [3] | 15 |
| 2-10 | Concentration and velocity profile for laminar flow on a plane plate according to the film theory. [15] | 17 |
| 2-11 | Mass transition according to two film theory: PB defines the phase boundary layer, c_k is the concentration in the bulk and c_g is the concentration at the phase boundary layer [3] | 19 |
| 2-12 | Influence of axial backmixing on theoretical separation units and balance line (\overline{BL}). \overline{EC} defines the equilibrium line and \overline{OL} defines the operation line. [3] | 21 |
| 2-13 | Tracer signal to measure axial back mixing [16] | 22 |
| 2-14 | Mass balance of finite volume element according to the dispersion model [16] | 23 |
| 2-15 | Design recommendations TCDC [18] | 25 |
| 3-1 | Installed TCDC 300; the space on the left side is used for the peripheral equipment | 29 |

| | | |
|------|--|----|
| 3-2 | TCDC 300 rotor | 30 |
| 3-3 | Modular plug system of the rotor | 30 |
| 3-4 | Stainless steel bearing plate with the installed friction bearing made of iglidur®X | 30 |
| 3-5 | TCDC 300 glass column with installed rotor | 31 |
| 3-6 | TCDC 300 disperser in the bottom glass part | 32 |
| 3-7 | Peripheral equipment: including pumps, valves for changing of operation mode and additional tank for closed circuit mode | 33 |
| 3-8 | Characteristic curve for centrifugal pump UP 130 [20] | 34 |
| 3-9 | Rotameter and digital display unit for hypersonic flow rate sensors; a: dispersed phase; b: continuous phase | 35 |
| 3-10 | Gear motor with installed coupling to connect the rotor to the motor | 36 |
| 3-11 | left: Display next to the control box showing rpm and circumferential speed; right: Display next to the gear motor for coarse adjustment of rotational speed | 36 |
| 3-12 | Flow sheet of TCDC 300 plant | 37 |
| 4-1 | TCDC 300 column at 150 rpm | 38 |
| 4-2 | TCDC 300 column at 200 rpm | 38 |
| 4-3 | Vortex formation at the aqueous phase outlet | 39 |
| 4-4 | left: Operating column with installed vortex breaker at the outlet of the aqueous phase; right: Detail of the vortex breaker installed at the outlet | 40 |
| 5-1 | Heights for measurement of dispersed phase holdup according to equation 5-11 [25] | 45 |
| 5-2 | Height of phase interface h_2 | 46 |
| 5-3 | Height of the continuous phase h_1 in the level gauge | 46 |
| 5-4 | Installed endoscope camera in detail | 47 |
| 5-5 | Installation endoscope camera at the TCDC 300 column | 47 |
| 5-6 | Picture of the endoscope camera with the rhodium reflector | 48 |
| 5-7 | Picture of the endoscope camera with the PTFE reflector | 48 |
| 5-8 | Sample picture of the automated pattern fitting algorithm | 49 |
| 6-1 | Increasing holdup; volumetric flowrate for picture a to f: $V_{org} = 355 \text{ l h}^{-1}$ and $V_{aqu} = 705 \text{ l h}^{-1}$; rotation speed: a=95 rpm, b=145,5 rpm, c=194 rpm, d=218 rpm, e=242 rpm, f=280 rpm | 51 |
| 6-2 | Hold up Data for TCDC 100 column with different hydraulic load and rotational speed [18] | 52 |
| 6-3 | Dispersed phase holdup for $B = 20 \text{ [m}^3\text{m}^{-2}\text{h}^{-1}\text{]}$ and $w/o = 0,5$ | 53 |

| | | |
|------|--|----|
| 6-4 | Dispersed phase holdup for $B = 20 [m^3m^{-2}h^{-1}]$ and $w/o = 0,67$ | 53 |
| 6-5 | Dispersed phase holdup for $B = 20 [m^3m^{-2}h^{-1}]$ and $w/o = 1$ | 53 |
| 6-6 | Dispersed phase holdup for $B = 20 [m^3m^{-2}h^{-1}]$ and $w/o = 1,5$ | 53 |
| 6-7 | Dispersed phase holdup for $B = 20 [m^3m^{-2}h^{-1}]$ and $w/o = 2$ | 54 |
| 6-8 | Gathered dispersed phase holdup according to operation parameters listed in table 6-1 for constant hydraulic load of $B = 20 [m^3m^{-2}h^{-1}]$. . . | 54 |
| 6-9 | Dispersed phase holdup at different w/o ratio and constant total hydraulic load of $B = 20 [m^3m^{-2}h^{-1}]$ including correlation according to Grafschafter and Siebenhofer [18] | 54 |
| 6-10 | Comparison of dispersed phase holdup in the TCDC 100 and TCDC 300 column at constant hydraulic load $B = 20 [m^3m^{-2}h^{-1}]$ [22] | 56 |
| 6-11 | Specification of probe levels [22] | 58 |
| 6-12 | Cumulative droplet size distribution for TCDC 100 column for varying rotational speed at constant w/o=1 and total hydraulic load of $B = 20 [m^3m^{-2}h^{-1}]$ [1] | 59 |
| 6-13 | Cumulative droplet size distribution for TCDC 300 column at probe level two for varying rotational speed at constant w/o=1 and total hydraulic load of $B = 20 [m^3m^{-2}h^{-1}]$ [22] | 59 |
| 6-14 | Predicted and measured Sauter mean diameter for TCDC 300 using correlation 2-47 [22] | 60 |
| 6-15 | Sauter mean diameter d_{32} probe level two for varying total hydraulic load B [22] | 61 |
| 6-16 | Sauter mean diameter d_{32} for different endoscope camera level Grafschafter et al. [22] | 61 |
| 6-17 | Probe level in one compartment | 62 |
| 6-18 | Comparison of Sauter mean diameter d_{32} TCDC 300 and TCDC 100 plotted over power per volume (P/V) | 62 |

List of Tables

| | | |
|-----|--|----|
| 2-1 | Empirical correlations for predicting the mean Sauter diameter in RDC columns including geometric specifications | 8 |
| 2-2 | Design parameter for hold-up correlation 2-49 | 27 |
| 3-1 | Rotor design TCDC 300 [1, 18] | 28 |
| 5-1 | Physical properties of the test system | 41 |
| 5-2 | Geometric design TCDC 300 | 42 |
| 5-3 | Exponent m for different scope of application. [23] In this Thesis constant P/V ratio is used | 42 |
| 6-1 | Operation points for hold up experiments | 52 |
| 6-2 | Fitted parameter for holdup prediction according to equation 2-49 [18] | 55 |
| 6-3 | Operation points for DSD determination at constant phase ratio: $w/o=1$ | 57 |
| 6-4 | d_{32} prediction parameters equation 2-46 fitted for the TCDC 300 column [22] | 59 |